The Planetary Science Journal, 4:131 (20pp), 2023 July https://doi.org/10.3847/PSJ/acd539

Post-flight Evaluation of Lidar-based Digital Terrain Models for OSIRIS-REx Navigation at Bennu

Jason M. Leonard[1], Jeroen L. Geeraert[1], Leilah K. McCarthy[1], Coralie D. Adam[1], Peter G. Antreasian[1], Olivier S. Barnouin[2], Michael G. Daly[3], Jeffrey A. Seabrook[3], and Dante S. Lauretta[4]
[1] KinetX, Inc., 950 W Elliot Road, Suite 220, Tempe, AZ 85284, USA; jason.leonard@kinetx.com
[2] The Johns Hopkins University of Applied Physics Laboratory, Laurel, MD 20723, USA
[3] The Centre for Research in Earth and Space Science, York University, Toronto, ON, M3J 1P3, Canada
[4] Lunar and Planetary Laboratory, University of Arizona, Tucson, AZ 85721-0092, USA
Received 2023 January 27; revised 2023 April 20; accepted 2023 May 12; published 2023 July 27

Abstract

The Origins, Spectral Interpretation, Resource Identification, and Security–Regolith Explorer (OSIRIS-REx) spacecraft spent more than 2 yr characterizing near-Earth asteroid (101955) Bennu. The OSIRIS-REx Laser Altimeter (OLA) was responsible for producing the most accurate reconstruction of the asteroid's surface—down to a global resolution of around 5 cm with a data precision of $\pm$1.25 cm. However, the best-quality global OLA digital terrain model (DTM), version 21 (v21), was not available for navigation during proximity operations, nor was the utility of this model evaluated for processing images and altimeter data for navigation. The focus of this paper is the post-flight assessment of the final OLA v21 DTM, its performance for navigation-related analysis, and estimates of corrections needed for the DTM and measurement models. We created 15 cm resolution maplets for processing optical navigation (OpNav) data, and 5 cm resolution DTMs for processing altimeter data, to estimate a combined spacecraft trajectory over five phases of the mission. Our estimated corrections to the OLA instrument model produce altimeter data residuals with a precision of 7.12 cm (1σ; one standard deviation from the mean). The OpNav maplets produce image residuals at 0.2 px (1σ) and estimated landmark locations accurate to $\pm$6 cm, outperforming DTM navigation-related performance requirements. Finally, our estimate of the global DTM scale is more precise and within 1.1σ of previously reported values. We find that a slight discrepancy persists between the image and altimeter data, with image data suggesting that the DTM is too small by 0.049%, but nevertheless is exceptional for navigation.

Unified Astronomy Thesaurus concepts: Orbit determination (1175); Near-Earth objects (1092); Small Solar System bodies (1469)

1. Introduction

The Origins, Spectral Interpretation, Resource Identification, and Security–Regolith Explorer (OSIRIS-REx) is a NASA New Frontiers–class asteroid sample return mission that arrived at near-Earth asteroid (101955) Bennu in late 2018 (Lauretta et al. 2017, 2019b). The road to successful sample collection took over 2 yr of proximity operations (ProxOps) at Bennu, which included the Navigation, Site Selection, and Sample Acquisition Campaigns (Lauretta et al. 2021). On 2020 October 20, the spacecraft performed the Touch-and-Go (TAG) sample-collection maneuver, retrieving loose material from the surface (Lauretta et al. 2022). The OSIRIS-REx spacecraft, including the collected regolith sample, departed the asteroid in May 2021 and is on its way back to Earth. The sample is expected to be back on Earth in September of 2023.

The Navigation Campaign consisted of the mission phases Approach, Preliminary Survey, and Orbital A (Lauretta et al. 2021). These phases were designed to provide initial images of Bennu, determination of Bennu's orientation, and initial estimates of Bennu's mass that were needed to navigate in subsequent campaigns. The Altimetry Working Group (AltWG) was responsible for building all digital terrain models (DTMs) for use in navigating the spacecraft during operations and for science evaluation. The preliminary images taken during the Navigation Campaign were used to build the initial global image-based stereophotoclinometry (SPC) DTM for use in optical navigation (OpNav; Gaskell 2001, 2002, 2011). Later, during the Site Selection Campaign, in the Detailed Survey phase, high-resolution imagery was taken. The imagery provided the data used to generate the operational image-based SPC DTMs, which were used to successfully navigate the remainder of the Site Selection Campaign (Orbital B, Orbital C, Reconnaissance A, and Orbital R phases) as well as the Sample Acquisition Campaign (Reconnaissance B through TAG).

Here we assess the final DTM generated from OSIRIS-REx Laser Altimeter (OLA) data and its performance for navigation-related analysis. While DTM products were generated from the OLA (Daly et al. 2017) instrument data collected during Orbital B (Barnouin et al. 2019, 2020), these were never used during operations for navigation. Both SPC and OLA DTMs provide a means to process landmark-based OpNav observables and light detection and ranging (lidar) observables for spacecraft navigation. Utilization of these observables and DTMs for navigation around small bodies introduces operational challenges, and care must be taken in identifying error sources in the models and the necessary parameters to estimate to correct for the modeling errors.

There are many known challenges to generating accurate DTMs and evaluating their performance as inputs for navigation. Through testing and previous small-body mission experiences, it has become known that uncertainties in the spacecraft trajectory can impact the global model size of Bennu due to errors in the apparent size of the body in the images. The OSIRIS-REx navigation team implemented lessons learned from the European Space Agency's Rosetta, another small-body mission with a 2014 rendezvous at comet 67P/Churyumov-Gerasimenko (67P; Muñoz et al. 2012). The Rosetta navigation team implemented an optical image-based navigation approach, similar to the SPC method used in operations for OSIRIS-REx (Gaskell 2022; E. Palmer et al. 2022, in preparation), and identified the need to iterate the model with the image-based DTM parameter estimates obtained from the orbit determination (OD) process (de Santayana & Lauer 2015). Preusker et al. (2015) improved upon the operational DTM by developing a high-resolution DTM of 67P. This updated model defined the final prime-meridian location and rotational elements of 67P along with the total volume, mass, and bulk density. The methods used by Preusker et al. (2015) did not include feedback from the OD process, and small discrepancies still exist when comparing it to the image-based DTM used for navigation (Godard et al. 2015, 2017). "Shadow navigation" efforts for Rosetta led by a Jet Propulsion Laboratory (JPL) navigation team also experienced considerable problems trying to disambiguate discrepancies between the overall size, mass, and landmark locations of 67P, directly impacting the ability to accurately navigate the spacecraft (Broschart et al. 2017). Broschart et al. (2017) also identified an issue with their SPC process and its inability to determine the offset in the center-of-mass to center-of-figure (COMCOF) of 67P.

The experiences from the Rosetta navigation and JPL shadow navigation teams were incorporated into the OSIRIS-REx OD concept of operations. These major error sources (global scale, offsets, orientation, mass, and landmark locations) were evaluated based on concern from previous small-body missions that experienced variations in the DTM parameter estimates through operations. In preparation for potential discrepancies between the dynamics and the baselined SPC DTMs used for navigation, the navigation team developed several Operational Proficiency Integrated Exercises and Navigation Training Exercises prior to ProxOps. The tests allowed for development in building SPC DTMs (E. Palmer et al. 2022, in preparation) and training to identify errors through the use of tracking data in the OD process (Leonard et al. 2017). This process proved critical in allowing the navigation team to estimate errors in the SPC DTM's pole axis, spin rate, the location of the prime meridian, as well as the shape scale factor and offset in the COMCOF (Adam et al. 2022a, submitted to this focus issue) producing a consistent global SPC DTM for science and navigation. The ability to predict the body-fixed location that was chosen for sample acquisition was dictated by the accuracy of the estimates of Bennu's SPC and OLA DTM parameters.

During OSIRIS-REx ProxOps, the OD team continuously evaluated SPC and OLA DTM deliveries from the AltWG to determine Bennu's rotational elements, offsets in the models, local landmark location errors, and global scale issues with the models (Leonard et al. 2019, 2020a). French et al. (2019) estimated early solutions during the Navigation Campaign for the gravity field and rotational elements of Bennu using a multiarc estimation method similar to the one developed by Godard et al. (2017) for Rosetta. This work provided an initial assessment to disambiguate discrepancies between the overall size (DTM scale errors) and mass of Bennu. Iteration between the OD team and AltWG continued through the Navigation Campaign to improve the DTM development while refining the scale errors and rotation state of Bennu based on OD estimates (Leonard et al. 2019, 2020a).

Not long into the Navigation Campaign, it was discovered that Bennu was actively ejecting small particles off of the surface (Lauretta et al. 2019a). Significant work went into the detection of the particles (Hergenrother et al. 2020), determining the location of the particle-ejection events (Leonard et al. 2020b; Pelgrift et al. 2020), and potential sources for the events themselves (Lauretta et al. 2019a). Once the particle tracks were determined and linked over multiple images, it was possible to derive a higher-fidelity gravity model (Mazarico et al. 2019; Chesley et al. 2020), improving the estimates obtained from satellite tracking alone (Scheeres et al. 2019, 2020). These independent estimates of the gravity field of Bennu were used in detangling the dependence on the accuracy of the Bennu DTMs and its correlation with the global scale factor to estimate the mass of Bennu accurately.

During the Site Selection Campaign, discrepancies between the global size and zonal variations were detected between the SPC DTM and the OLA DTM (Al Asad et al. 2021; Seabrook et al. 2022). A calibration error was detected in the OLA mirror and corrected for in subsequent OLA DTMs (Seabrook et al. 2022), but a global size discrepancy still existed between the SPC and OLA DTMs. Recon B allowed for an opportunity to perform a flight activity to test the consistency between the OLA's High-Energy Laser Transmitter (HELT) and Low-Energy Laser Transmitter (LELT) modes (Daly et al. 2017). During this time, a bias between the HELT and LELT modes was identified, the first indication that a significant bias could be present in the returned range from the OLA instrument. Due to these issues, the OLA DTM was never assessed for use in navigation products.

The verification of the final OLA DTM constructed by AltWG, version 21 (v21), and its performance for navigation-related analysis are the focus of this paper. The procedures developed prior to and during operations, and the lessons learned throughout, provide the foundational tools for this analysis. Throughout the paper, imaged-based DTMs constructed with the SPC program are denoted as SPC v(n), while OLA-based DTMs that used only lidar data are denoted as OLA v(n). The improvements in the construction of the OLA v21 DTM are analyzed for the first time through the use of image-based landmark navigation data, combined with OLA lidar data, and radiometric tracking data through the OD process. Comparisons to pre-ProxOps DTM performance metrics concerning navigation-related analysis as well as requirements imposed on the DTM during the mission are assessed. Estimates of the modeling parameters used to compute the landmark and lidar observations are given, as well as an assessment of the quality of the navigation data and the DTM products. Four orbital phases (Orbital A, B, C, and R) and a reconnaissance phase (Recon B) from the OSIRIS-REx mission (Lauretta et al. 2021) are analyzed independently and ultimately combined to provide a consistent solution for the estimated camera models, lidar models, and DTM parameters.

2. Navigation Data

The OSIRIS-REx spacecraft collected three primary navigation data types: radiometric data, optical image data, and lidar data. Radiometric data were collected from the Deep Space Network (DSN) and included Doppler, range and delta-differenced one-way range (DDOR; Moyer 2005). Image data were collected by Navigation Camera (NavCam) 1 and NavCam 2 from the Touch-and-Go Camera System (TAGCAMS; Bos et al. 2018), as well as by MapCam and PolyCam from the OSIRIS-REx Camera Suite (OCAMS; Rizk et al. 2018; Golish et al. 2020). Lidar data were acquired primarily from the OLA instrument (Daly et al. 2017), except in the case of some test data from the Guidance, Navigation, & Control (GNC) lidar system (Church et al. 2020).

2.1. Radiometric Data

Radiometric range, Doppler, and DDOR observations were the primary sources of navigation data used during outbound cruise (Antreasian et al. 2018, 2019) and were supplemental to image data taken during ProxOps. Ranging data were collected on the high-gain antenna throughout ProxOps and on the low-gain antenna when the data link could be closed. Doppler data were collected consistently throughout ProxOps with the frequency of multiple tracking passes per day for the majority of operations. DDOR were infrequently used for navigation purposes and had the main effect in determining Bennu's heliocentric orbit. The quality of the tracking data was better than anticipated (Antreasian et al. 2022).

2.2. Optical Images and Landmark Navigation

Optical image data from NavCam 1 and MapCam were used throughout the mission phases. Precision modeling of the camera intrinsic parameters is vital when utilizing optical images for navigation around small celestial bodies. Calibration of the camera lens distortion reduces errors in the predicted locations of surface features used for navigation purposes. The location of the camera pupil is also necessary in accurately computing the landmark location. The mathematical model used for image-based navigation is similar to that presented by Owen (2011). Landmark maplets are correlated with an image of the relevant surface that has been ortho-rectified into the DTM frame (Gaskell 2001, 2002, 2011). Adam et al. (2022a) provide an overview of the use of SPC for navigation on OSIRIS-REx, while Adam et al. (2022b) give a concise overview of the planning and execution of imaging sequences to obtain OpNav data.

Extensive calibration of the NavCam 1 imager was conducted throughout operations using stellar images to check the distortion of the lens, thermal effects on the cameras focal length and boresight, and trending of the onboard attitude estimates from the star trackers (Pelgrift et al. 2018; Bos et al. 2020). The intrinsic parameter calibrations of NavCam 1 and 2 resulted in a noise over the detector of around 0.08 px (1σ; one standard deviation from the mean) in each coordinate. Throughout operations, a majority of the NavCam 1 sequences involved a corresponding pair of long- and short-exposure images taken during an inertial hold attitude after a specified settling time to remove errors induced by the spacecraft slewing. Long-exposure images allowed for background stars to be visible with the knowledge that Bennu's surface would be overexposed, washing out any detectable features. A subsequent short-exposure image proceeding the long-exposure image was used to resolve surface features to correlate with a known set of landmarks. The combination of long- and short-exposure navigation images helped to remove any unknown pointing errors associated with the camera direction relative to inertial space. During the Detailed Survey phase of the mission (Lauretta et al. 2021), it was discovered that the NavCam boresight would shift slightly when OLA was turned on (Sahr et al. 2022). OLA's thermal dissipation would warp the instrument deck and could be seen in the temperature increase in nearby instrument sensors.

Table 1
NavCam and MapCam Landmark GSD Per Mission Phase

Mission Phase	Range to Surface (m)	NavCam Resolution (cm px^{-1})	MapCam Resolution (cm px^{-1})
Orbital A	1299–1832	37.4–52.7	8.83–12.5
Orbital B	597–786	17.2–22.6	4.06–5.34
Orbital C	1351–1803	38.9–51.9	9.19–12.3
Orbital R	838–1211	24.1–34.9	5.70–8.23
Recon B	584–1227	16.8–35.3	3.97–8.34

Note. See Lauretta et al. (2021) for a timeline and description of OSIRIS-REx operational phases.

During operations, however, inconsistency between imager data lead the team to reevaluate the epoch at which NavCam was assumed to take an image. Adam et al. (2022a) discusses the rolling shutter issue with NavCam 1 and how it was corrected. The rolling shutter resulted in two main timing impacts on the OpNav data processing. Nominally, the image should be time-tagged at the midpoint of the image exposure interval, but was reported on the image as the start of the readout inducing an error of almost 0.5 sec. During operations the time-tag error was inherent in all navigation-related products and publications prior to TAG reconstruction work and results presented in Leonard et al. (2022). The next issue is that the CMOS detector does not have an instantaneous readout time across all of the rows in the detector. The readout of the CMOS detector is such that it reads out row-by-row and it takes over a second from the start of a readout to completely reading the image. This induces a smearing on the images. In addition, the readout duration exposes landmarks at different times. This error produces landmark OpNav errors up to 1 px during orbital phases. All images in this analysis use the most current assumptions for the best practices in modeling the TAGCAMS and OCAMS imagers.

Different mission phases provided different viewing conditions and resolutions of landmarks throughout ProxOps. The range to surface distances, ground sample distances (GSDs), and resolutions for NavCam and MapCam are shown in Table 1. A wide range of resolutions are available from the mission phases analyzed in this work.

2.3. Lidar Data

The OLA instrument on board the OSIRIS-REx spacecraft was contributed by the Canadian Space Agency and managed by the AltWG. Compared to the GNC lidar, OLA was the most precise of the ranging instruments on board OSIRIS-REx and was used in the generation of scientific DTMs for the mission. OLA was utilized during operations to provide ranging to the surface of Bennu at unprecedented spatial scales for a planetary mission (Seabrook et al. 2019).

OLA is a two-dimensional scanning lidar that has two laser emitters and operational modes. The high-energy mode, known

Table 2
OLA Performance Requirements

Mission Phase	Range to Surface (m)	Range Accuracy (cm) 1σ	Range Precision (cm) 1σ
Preliminary survey	6750	50	30
Detailed survey	4750	50	30
Orbital A	1250	50	30
Orbital B	750	30	13
Reconnaissance	500	30	4

Note. See Lauretta et al. (2021) for a timeline and description of OSIRIS-REx operational phases.

as HELT, was used for ranging at distances from Bennu between 1 and 7.5 km with a data rate of 100 Hz. The low-energy mode, LELT, operated at a higher data rate of 10 kHz and was used for ranging at distances between 500 m and 1 km. The HELT mode was used during the Preliminary Survey, Orbital A, and Recon B phases, while the LELT mode was used primarily during Orbital B, as well as for some data collected in Recon B.

OLA data are provided in various levels of refinement throughout the processing pipeline. This work uses the Level 2 data, which have been processed on the ground for updates in the timing conversion of the time-tag and corrections to the lidar data itself. The data used in this analysis additionally have updated corrections to the mirror scaling and polynomials, as well as the wave corrections in the slow scanning axis, as described in Seabrook et al. (2022). The OLA performance requirements for various phases and distances are given in Table 2. The range accuracy is a measure of the how close the measured range is to the real value (i.e., is it biased) and the range precision is a measure of the repeatability of the measurement (i.e., the noise).

2.3.1. Ray-traced Lidar Intercept

The mathematical implementation in the operational OD software for a single lidar return intercept location of a surface model such as a DTM is given in Leonard et al. (2022). The model assumes that the emission time, t_e, is known and that the computed lidar range, ρ, is calculated as half the total round-trip delay as

$$\rho = \frac{c}{2}(\tau_d + \tau_u + \delta_{\text{clock}}) + b_L, \tag{1}$$

where c is the speed of light, τ_d is the down-leg light time from the lidar to the surface, τ_u is the up-leg light time from the surface to the detector, δ_{clock} is the delay due to the difference in time due to clock drift, and b_L is the bias in the instrument. The light-time surface intercept location is iteratively solved for until convergence using the DTM. Once the down-leg light time is known, the up-leg light time is iteratively solved for to determine the total round-trip light time in Barycentric Dynamical Time (TDB).

2.3.2. Point-cloud Projection

Lidar point clouds have been generated at planetary bodies for a variety of analyses (Rowlands et al. 1999; Mazarico et al. 2010; Xiao et al. 2021; Leonard et al. 2022). The OD software utilizes a lidar point-cloud measurement model that is consistent with the ray-traced surface intercept model (Leonard et al. 2022) and is performed in the TDB spacetime reference frame. Xiao et al. (2021) introduces four methods at varying levels of fidelity to produce point clouds around planetary bodies. The implementation in this analysis uses a formulation similar to the pointing aberration model and special relativity model given in Xiao et al. (2021).

OLA's recorded observed range value is given in Equation (1) as half the measured round-trip light time. The outgoing lidar direction is corrected for aberration. The down-leg and up-leg light times are solved for without assuming a constant velocity assumption. Once the down-leg light time is known, the intercept location is determined.

2.4. Shape Modeling

During operations at Bennu, the AltWG was responsible for delivering two SPC-based DTMs for navigation purposes. The 75 cm resolution SPC v20 DTM was created using Approach and Preliminary Survey image data and was used in operations between Orbital A and Orbital B (Leonard et al. 2019, 2020a; Al Asad et al. 2021) and initial evaluation of Bennu's shape (Barnouin et al. 2019). An interim, SPC v32 DTM, was used for most of Orbital B and C. The final SPC-based navigation model, the 35 cm v42, was used for the remainder of the OSIRIS-REx mission.

Each iteration of SPC DTM was known to introduce discrepancies in the location of the prime meridian, the body-fixed reference frame coordinates, and variations in the scale or global size of the body (Leonard et al. 2019, 2020a). With each new DTM delivery, the accuracy of the landmark locations, reference frame offsets, and global scale error were assessed and delivered to AltWG to update the model. Throughout operations, the models were recentered on the current best estimate of the COMCOF of the model. The final SPC v42 DTM radius was determined to be too large by nearly 50 cm by the OD team during operations using tracking data and multiphase estimations. Al Asad et al. (2021) performed image comparisons that indicated that the v42 model was too small, but the OLA-based DTM at the time suggested it was too large. These discrepancies led to a concentrated effort to attempt to resolve global scale issues with the developed models.

2.4.1. SPC-based DTMs

The SPC-based DTMs developed during the OSIRIS-REx mission are discussed in Al Asad et al. (2021). The SPC v42 global DTM set was extensively used and assessed throughout ProxOps and became the primary navigation model for the mission beginning in the Recon A phase. TAG-related DTM products were correlated and adjusted to match this model, thus the prime meridian used throughout operations was aligned with this model. All final planetary constants kernels (PCKs) delivered to the project and externally are referenced to this SPC v42 DTM and its defined prime-meridian location.

An overview of the AltWG process for building SPC-based DTMs is given in Barnouin et al. (2020) and Palmer et al. (2022). The global size issues discussed in Al Asad et al. (2021) were an expected issue for the mission based on Rosetta experiences. During Approach, errors in the spacecraft trajectory, in conjunction with the insensitivity to the apparent size of Bennu at 10–60 km away, resulted in scale errors in the earlier image-derived DTMs that continuously fed through to the final SPC v42 DTM.

The SPC v42 DTM set has 134 1.2 m resolution landmarks, 309 75 cm resolution landmarks, 1881 35 cm resolution landmarks, and one 14 cm resolution landmark that were used for navigation during ProxOps at Bennu. The landmark locations are tiled across the surface of Bennu with a spacing such that each associated DTM shares 30% overlap with each adjacent landmark DTM. Typically, for operations, a ratio of image resolution (m px^{-1}) to DTM scale of 3 was used in determining which maplets to use. At certain points during the mission, this ratio was relaxed up to a ratio of 9 in order to obtain landmarks capable of correlation (McCarthy et al. 2022). The performance of the SPC v42 model for navigation is detailed in McCarthy et al. (2022), who show that it exceeded expectations of preflight analysis.

2.4.2. OLA-based DTMs

During the Orbital B mission phase, nearly 5 weeks of operations were dedicated to the global mapping of Bennu with the OLA LELT mode (measurement rate of 10 kHz). This mapping was primarily used in the generation of a global DTM of Bennu. Seabrook et al. (2019) describes, in detail, the approach taken to use overlapping raster scans to reduce the dependence of this global DTM on absolute position and pointing knowledge. Overlapping raster scans acquired during the Orbital B mapping phase had an average spot spacing of 5 cm globally, except for areas where shadows or cliffs existed. Differencing overlapping OLA scans showed that the precision of the OLA data was on the order of ± 1.25 cm (Daly et al. 2020). Seabrook et al. (2022) improved upon previous modeling of OLA by removing known errors in the instrument to produce the final OLA v21 DTM. Comparison of the SPC v42 DTM to the OLA v21 DTM indicates that the former is larger by 44 cm radially (Seabrook et al. 2022).

For processing lidar data, the OLA v21 DTM triangular mesh DTMs were used, which have a spatial resolution of 5 cm. No alteration to the triangular mesh model was performed in processing the data. The data set consists of 800 OBJ/DSK files that represent the topography of Bennu with slightly overlapping regions. Seabrook et al. (2022) details the quality of the OLA v21 DTM, with analysis indicating the lidar data set produced a median global standard deviation of 2.74 cm. Scale-invariant feature transform keypoints and descriptors (unique model features, similar to a landmark) were used to identify matching features between the image and renderings of the OLA v21 DTM with an average keypoint residual on the order of 4 cm, suggesting that the OLA v21 DTM was accurate to this scale.

The OLA v21 DTM was used to generate 2500 landmarks with a maplet resolution of 15 cm GSD for use in the SPC process to correlate OpNav landmarks. Albedo data are necessary to obtain decent correlations in the SPC process so a smoothed-albedo model was used. The smoothed-albedo model is a modified Lommel–Seeliger function developed for the Moon that provides reasonable renderings when compared to images of Bennu (Seabrook et al. 2022). All mission phases analyzed in this work used this updated model with reprocessed OpNav landmark data that were not available during ProxOps at Bennu.

3. Overview of Mission Phases Analyzed

The OSIRIS-REx mission consisted of several flyby, orbital, and reconnaissance phases during ProxOps at Bennu (Williams et al. 2018; Antreasian et al. 2022). Flyby data obtained during the Preliminary and Detailed Surveys were vital in initial characterization and evaluation of the primary data types used for navigation. High-resolution PolyCam and MapCam imagery taken during these phases was used to build the primary SPC-based DTMs. The narrow field of view of these imagers, combined with the hyperbolic trajectory, did not allow for an accurate assessment of the DTM from navigation data.

The orbital phases of the mission provided extensive imagery with various resolutions and phase angles to properly assess the DTMs developed during the mission. The precision of the OpNav data could be determined through the diverse observing conditions experienced during the orbital phases. Lastly, the reconnaissance phases offered the opportunity for close-range, very-high-resolution local observations of the mission's primary and backup sample sites. In this work, we utilize data from the orbital and Recon B phases to assess the navigation performance of the DTMs.

3.1. Orbital A

During Orbital A (2019 January and February), the first orbital phase of the mission, the spacecraft orbited in a 2.1×1.5 km frozen orbit with a period of approximately 62 hr. This mission phase marked the end of the Navigation Campaign, at which time the spacecraft went through perihelion. During this time frame, the Navigation Team learned to navigate the spacecraft with radiometric and optical image data. The transition from center-finding OpNav to landmark-based OpNav occurred on 2019 January 25.

During this phase, the nominal OpNav frequency with NavCam 1 was roughly every 2 hr, with a 2×1 mosaic at each epoch. The discovery and monitoring of naturally ejected particles (Lauretta et al. 2019a) required an increase in this OpNav cadence to a set of images every 30 minutes. Each set of NavCam 1 images contained a corresponding stellar image that was used to obtain the inertial attitude of the camera at the image epoch.

The spacecraft performed nominally during this phase with minimal errors from unmodeled accelerations. The solar arrays were oriented at the 90, 45 configuration (canted 45° forward from the $+Z$-axis of the spacecraft). This was the nominal cruise configuration for the solar arrays, inducing a significant acceleration in the $+Z$-axis of the spacecraft, which was oriented at nadir throughout the majority of Orbital A. Earth-point attitudes occurred for nearly 5 hr every day to downlink the day's OpNav images and other spacecraft data.

The final few weeks of Orbital A and the transition to Detailed Survey saw the use of OLA's HELT mode, which completed nine scans of Bennu's surface covering mostly the poles. Initial estimates of the mass, rotational state, and discrepancies with the DTM scale and landmark locations were obtained. The HELT data acquired during this phase were not used in the construction of the OLA v21 DTM (Seabrook et al. 2022) analyzed in this work. MapCam images were also taken during the Orbital A phase; however, no corresponding stellar imaging occurred, thus the attitude of the camera at the imaging epoch was degraded.

3.2. Orbital B

Orbital B (2019 June to early August) was a 925 m near-circular orbit that was primarily used for globally mapping the surface of Bennu. As in Orbital A, NavCam 1 was used for landmark OpNav throughout the phase. Images were taken every 2 hr, without the 2 × 1 mosaics used in the Orbital A phase. The solar arrays were moved during the Detailed Survey phase to 90, 20 (canted 20° forward from the +*Z*-axis of the spacecraft) and nominally stayed in this orientation for the remainder of ProxOps. This change in the nominal configuration of the spacecraft reduced the +*Z*-axis acceleration due to the solar panels and pushed the spacecraft further back into the terminator plane for orbital phases.

OLA's LELT mode was used during this phase to map Bennu with average spot spacings below 5 cm globally (Daly et al. 2020). Eight-hundred and ninety-two raster scans were performed between 2019 July 1 and August 5, with a single scan having an approximate footprint of 120 × 120 m on the surface. Each scan took about 5.5 minutes and produced nearly 3.3 million range returns. The 892 raster scans performed in Orbital B were used in the construction of the OLA v21 DTM (Seabrook et al. 2022).

3.3. Orbital C

The Orbital C phase (2019 August and September) put the spacecraft in a similar frozen orbit to that flown in Orbital A, at 1.9 × 1.6 km. The purpose of this phase was to reduce operations and allow the OSIRIS-REx team to recuperate for a month from the high-intensity cadence of operations performed to that point.

NavCam 1 was the sole source of OpNav images taken during the phase. Similarly to the previous orbital phases, an image was taken roughly every 2 hr. The nominal attitude was nadir-pointed, except for 5 hr each day when the spacecraft slewed to Earth-pointed to downlink data. The main differences in the dynamics of Orbital C compared to Orbital A were the Sun distance (aphelion during Orbital C, perihelion during Orbital A) and the solar array 90, 20 configuration maintained throughout Orbital C, reducing the +*Z*-axis acceleration.

3.4. Orbital R

Orbital R (late 2019 October to early 2020 January) was similar to Orbital B in duration, orbit size (1.4 × 1.1 km), and OpNav cadence. The major difference between the two orbital phases was Sun distance: Orbital R overlapped with perihelion. MapCam images taken during the end of Orbital R were used in the OD process in addition to the nominal cadence of NavCam 1 images. The addition of MapCam provided higher-resolution images to compare with the landmarks derived from NavCam 1 images. The higher resolution and the ability to combine landmark data from two imagers provided a better estimate of the spacecraft's radial distance to Bennu.

3.5. Recon B

As the mission closed in on sample collection, the landmark locations and touchdown coordinates that would be used by the onboard autonomous navigation system (Norman et al. 2022; Olds et al. 2022) to fly the TAG trajectory needed to be updated based on the latest shape information. Yet significant discrepancies were found between the SPC and OLA DTMs. At this time, the Orbital A OLA HELT data indicated that the SPC v42 DTM was too large by up to 1% volume (1–1.5 m radius). However, image renderings of the OLA DTMs developed using Orbital B LELT data did not agree well when compared to images taken on the Approach phase. The rendered images using the DTMs showed that the model was too tall along Bennu's polar axis and too small along Bennu's equator (Seabrook et al. 2022). These model errors directly impacted two mission requirements. First, the TAG site vertical height in the plane of the DTM needed to be known to less than 14 cm rms. Second, the vertical height rms with respect to the landmarks used by the autonomous navigation system also needed to be known to less than 14 cm. At this point in the mission, the absolute accuracy of the target TAG site was known to within 1 m rms, with uncertainties of 1 m or more depending on latitude. Because of these impacts to the mission requirements and landmark locations, the scale discrepancy between the OLA and SPC models was a high-priority issue for the mission.

To mitigate this issue, the navigation and AltWG teams developed a plan to take off-nadir OLA scans of the asteroid during the Recon B mid-altitude flyovers of the primary and backup sample sites (2020 January and February). Alternating HELT linear and LELT raster scanning observations were planned to ride along with MapCam OpNav and particle imaging sequences, where the spacecraft slewed to point the MapCam boresight 5° toward the Sun from nadir while in the 1 × 1.4 km terminator orbit between flyovers. These off-nadir lidar data would help evaluate the source of the scale issue, because the residual signatures are different for scale errors, orbit radial errors, and fixed range biases as a function of nadir angle.

While these plans were being made, the AltWG discovered a 0.73% scale error in the reported azimuth angles of the scanning mirror when comparing the lidar-derived models with image data (Daly et al. 2020; Seabrook et al. 2022). To further verify this discovery and provide a data set to help calibrate the scan mirror, three observation sequences were designed to collect data from various OLA scan orientations while the spacecraft was off-nadir pointing. Each sequence was performed three times per day from 2020 January 27 to February 10: (i) HELT linear scan in line with the spacecraft slew direction, full extent of the scan mirror in azimuth (∼12° off-nadir, max); (ii) HELT linear scan perpendicular to spacecraft slew direction, full extent of the scan mirror in elevation (∼5° off-nadir, max); and (iii) LELT raster scan with fast axis aligned with the spacecraft velocity, all other parameters the same as in Orbital B (∼10° off-nadir, max).

4. Estimation Setup

The operational OD filter used for navigation was the Multiple Interferometric Ranging Analysis using GPS Ensemble (MIRAGE) navigation software (Guinn & Wolff 1993). MIRAGE is a pseudo-epoch state batch sequential filter used to estimate the spacecraft state, stochastic parameters, and bias parameters impacting the spacecraft trajectory and measurements.

Each mission phase analyzed is considered disjointed in time and independent when considering the spacecraft state. No constraints are applied to dynamically link the spacecraft states between phases and no overlapping trajectory spans exist in the analysis. Individual estimates for local phase parameters and

Table 3
Analysis Data Span and Types Used by Mission Phase

Mission Phase	Data Start	Data End	Data Used
Orbital A	2019 February 1	2019 February 28	Doppler, NavCam 1, MapCam, HELT
Orbital B	2019 June 28	2019 August 6	Doppler, NavCam 1, LELT
Orbital C	2019 August 9	2019 September 17	Doppler, NavCam 1
Orbital R	2019 November 1	2020 January 14	Doppler, NavCam 1, MapCam
Recon B	2020 January 14	2020 February 14	Doppler, NavCam 1, MapCam, HELT, LELT

global parameters are provided as well as a combined solution using techniques similar to those presented by Godard et al. (2017), French et al. (2019), and Goossens et al. (2021).

The Bennu ephemeris and uncertainties used for this analysis is the JPL Solution 118 (Farnocchia et al. 2021). No corrections to the ephemeris are made since the JPL Solution 118 used data throughout the duration of ProxOps. In addition, ranging and DDOR data are not utilized in this analysis due to the fact that during ProxOps they mainly contribute to the estimation of the Bennu ephemeris. Range and DDOR data are removed in order to not double-count the data in the estimation of the spacecraft, as suggested by the JPL Solar System Dynamics group.

The gravity model of Bennu used throughout the analysis is based on a combined solution from the particle-ejection events and spacecraft radiometric and image data. The solution was generated during operations in a similar manner to the methods used by Mazarico et al. (2019) and Chesley et al. (2020). A $9° \times 9°$/order gravity model with inclusion of the J10 estimate is used. Only the gravitational parameter (GM) of Bennu is estimated in this work, keeping the remaining gravity field terms held fixed. Scheeres et al. (2019) and Scheeres et al. (2020) provide statistically consistent solutions for the gravity field based on particle- and spacecraft-derived values for the mass of Bennu. However, significant correlations between GM estimated with landmark data and the DTM used are known to exist. The estimation of the GM from landmark OpNav data is directly correlated with the global shape scale. Goossens et al. (2021) attempted to remove this correlation through the use of difference measurement types but determined that a previously derived OLA v20 DTM (Daly et al. 2020) was too small by ∼25 cm at the equator, or a scale factor of 1.000896 ± 0.00036.

Table 3 gives the duration of the data spans used for each phase of the mission that is analyzed. In addition to the data span, it also indicates which data were used during the OD process. Typically, Doppler data are weighted based on the rms of the pass and scaled around 3× to account for noise due to turbulent processes on various timescales (McElrath et al. 2004; Antreasian et al. 2005).

4.1. DTM Orientation and Offset

The local reference frame of the DTM does not necessarily align with the principal-axis frame of Bennu. This offset is usually the result of the DTM building process and how the prime meridian and spin axis are defined. Once the prime meridian is decided from the DTM process and the body-fixed axes of the model are defined, a translational offset and an offset in the orientation relative to the true principal axis of the body exist. A landmark, or a point on the surface, in the principal-axis reference frame can be expressed as

$$\boldsymbol{r}_L^P = C[\boldsymbol{R}_S^P]\boldsymbol{r}_L^S + \boldsymbol{r}_{\mathrm{CF}}^P, \tag{2}$$

where C is the global DTM scale factor, $[\boldsymbol{R}_S^P]$ is the transformation from the principal-axis frame (P) to the DTM frame (S), $\boldsymbol{r}_L^S$ is the location of the landmark in the S-frame, and $\boldsymbol{r}_{\mathrm{CF}}^P$ is the constant COMCOF expressed in the P-frame. The DTM transformation $[\boldsymbol{R}_S^P]$ represents the constant offset between the spin axis and the DTM reference coordinate system and is estimated as a set of yaw-pitch-roll (3-2-1 Euler angle) corrections.

4.2. Camera Parameters

The OD implementation for the imagers allows for estimation of the camera location, camera-to-spacecraft reference frame, spacecraft-to-inertial reference frame parameters, and time-tag errors. Errors in the spacecraft center-of-mass location can be estimated based on the imager data. Landmark images allow for estimation of landmark location errors, DTM frame offset from the principal-axis frame, the COMCOF of Bennu, a global scale correction to the DTM, and a spherical-harmonic-based correction to the shape of Bennu.

4.3. Lidar Parameters

OLA measurements are time-tagged at the transmission time, with the observable being half of the round-trip light time to the surface. The OLA measurement model implemented in MIRAGE allows for estimation of the lidar location, boresight direction and orientation relative to the spacecraft reference frame, scaling in the mirror coordinate system of azimuth/elevation output, constant bias, and errors in the onboard oscillator. Each OLA mode (HELT and LELT) are treated as individual instruments having unique estimates for each of the governing parameters.

In addition to the lidar-specific parameters, the implementation also allows for estimation of the spacecraft center-of-mass location, spacecraft-to-inertial reference frame parameters, the COMCOF of Bennu, DTM frame offset from the principal-axis frame, and a global scale correction to the DTM.

4.4. Orbit Determination Strategy

Table 4 gives the OD setup and a priori sigmas implemented in the MIRAGE filter used in this analysis. Finite burns are only estimated during the Recon B phase as no maneuvers were present in the durations analyzed in the Orbital phases. Stochastic accelerations are estimated in the spacecraft body-fixed reference frame to account for any mismodeling in the dynamics of the spacecraft and environment. An acceleration error is estimated when the spacecraft remained at Earth-point attitude for high-gain antenna contacts. When stellar image epochs were near OpNav landmark images, the pointing of the camera was not estimated. Camera frame corrections are estimated when no stellar images are available as a constant

Table 4
Orbit Determination Estimated Parameters and a Priori Uncertainties

Parameter Type	Error Source	A Priori Uncertainty 1σ	Correlation Time	Update Time
Dynamic	Spacecraft state			
	Position	(10 m, 10 m, 10 m)	⋯	⋯
	Velocity	(0.5 mm s^{-1}, 0.5 mm s^{-1}, 0.5 mm s^{-1})	⋯	⋯
Stochastic	Spacecraft body frame accelerations			
	X	5.0e–13 km s^{-2}	0	3 hr
	Y	1.0e–13 km s^{-2}	0	3 hr
	Z	5.0e–13 km s^{-2}	0	3 hr
	OLA LELT yaw/pitch/roll	0	0	Every scan
	OLA HELT yaw/pitch/roll	0	0	Every scan
	NavCam 1 yaw/pitch/roll	0	0	Images w/o stars
	MapCam yaw/pitch/roll	0	0	Images w/o stars
Constant bias	Solar pressure			
	Scale factor	0.05	⋯	⋯
	Solar array specular	0.01	⋯	⋯
	Earth-point acceleration	1.0e–12 km s^{-2}	⋯	⋯
	OLA LELT			
	Yaw/pitch/roll	0.01 deg	⋯	⋯
	Bias	50 cm	⋯	⋯
	OLA HELT			
	Yaw/pitch/roll	0.01 deg	⋯	⋯
	Bias	50 cm	⋯	⋯
	NavCam 1 yaw/pitch/roll	0.01 deg	⋯	⋯
	MapCam yaw/pitch/roll	0.01 deg	⋯	⋯
	Shape model			
	Scale factor	1.0e-3	⋯	⋯
	COMCOF	(5 cm, 5 cm, 5 cm)	⋯	⋯
	Frame pitch	0.01 deg	⋯	⋯
	Frame roll	0.01 deg	⋯	⋯
	Bennu GM	5.0e–12 km^3/s^2	⋯	⋯
	Bennu orientation			
	R.A.	0.01 deg	⋯	⋯
	decl.	0.01 deg	⋯	⋯
	Prime meridian	0.05 deg	⋯	⋯
	Rotation rate	1.0e-9 deg/s	⋯	⋯
	Finite burns			
	R.A.	Gates (1963)	⋯	⋯
	decl.	Gates (1963)	⋯	⋯
	Thrust	Gates (1963)	⋯	⋯
	Desaturation maneuvers	(0.2 mm s^{-1}, 0.2 mm s^{-1}, 0.2 mm s^{-1})	⋯	⋯
	Landmark vector	(1.0 m, 1.0 m, 1.0 m)	⋯	⋯
Consider	Spacecraft center-of-gravity	(1 cm, 1 cm, 5 cm)	⋯	⋯
	Bennu ephemeris	Farnocchia et al. (2021)	⋯	⋯
	DSN station locations	Slobin (2022)	⋯	⋯
	UT1	2.5 cm	⋯	⋯
	Pole X, Y	(0.2 cm, 0.2 cm)	⋯	⋯
	Troposphere			
	Wet	1 cm	⋯	⋯
	Dry	1 cm	⋯	⋯
	Ionosphere at S-band			
	Day	5.5 cm	⋯	⋯
	Night	1.5 cm	⋯	⋯

offset in the camera reference frame. Due to the warping of the image deck from increased thermal output of OLA, a constant MapCam reference frame offset is estimated during those times over all MapCam images.

5. Evaluation of the OSIRIS-REx Laser Altimeter v21 Digital Terrain Model for Navigation

The data presented in Table 3 from individual mission phases were used to estimate global corrections to the OLA v21

Table 5
Estimation Results for OLA v21 DTM Reference Frame Translation and Rotation Offset

Estimated Parameter	Orbital A	Orbital B	Orbital C	Orbital R	Recon B	Combined
$\boldsymbol{r}_{CF}^{P}$ X (cm)	4.69 ± 0.10	4.99 ± 0.07	4.71 ± 0.41	4.80 ± 0.09	4.94 ± 0.08	4.85 ± 0.05
$\boldsymbol{r}_{CF}^{P}$ Y (cm)	-3.02 ± 0.10	-2.99 ± 0.07	-2.99 ± 0.41	-2.97 ± 0.09	-3.08 ± 0.08	-3.12 ± 0.05
$\boldsymbol{r}_{CF}^{P}$ Z (cm)	-7.84 ± 1.42	5.28 ± 0.42	6.63 ± 6.64	6.00 ± 0.01	-4.66 ± 1.38	4.72 ± 0.42
Pitch (mdeg)	23.91 ± 0.25	24.85 ± 0.22	23.32 ± 1.20	25.16 ± 0.26	24.68 ± 0.21	25.25 ± 0.15
Roll (mdeg)	-6.64 ± 0.25	-6.14 ± 0.23	-5.18 ± 1.18	-5.55 ± 0.25	-5.08 ± 0.21	-5.78 ± 0.15

DTM (translation and orientation) and to the OLA HELT and LELT modes. The consistency between the common estimated parameters from separate mission phases provides some insight into the information gained from the data in that phase. Variations between phases give some indication of the disparity of the data. A combined solution using all of the phases provides the best estimate of the parameters governing the spacecraft, DTM, and instruments themselves.

Once a combined solution is estimated, the overall performance of the OLA v21 DTM can be evaluated. The statistics across multiple phases in the OpNav and OLA data elucidate the performance of the instruments and of the DTM when used to process those observations. The following results provide information on the performance of the OLA v21 DTM and final estimated corrections needed to accurately model the instrument.

5.1. Estimated OLA v21 DTM and OLA Instrument Model Corrections

OLA data were used to fit the trajectories during Orbital A (HELT mode only), Orbital B (LELT mode only), and Recon B (both HELT and LELT modes). The Orbital A data set is limited in its coverage of Bennu. A majority of the data points intercept in higher-latitude regions, with a few scans extending around the equator. The spacecraft slewed to take OpNav data during OLA data acquisition, incurring large pointing errors during the slew periods. These data were removed from analysis. The Orbital B data set, which was used in the generation of the OLA v21 DTM, was unaltered except for the removal of gross outliers. This is also the case for the Recon B OLA observations, which were designed to produce larger off-nadir variations in the data that were not seen in the Orbital B data set.

The COMCOF and a constant DTM frame offset were consistently determined from each individual phase, as shown in Table 5. The COMCOF X and Y vector components were well determined from each individual phase with estimates consistent to within several millimeters. The Z component of the COMCOF was the most uncertain. Equation (3) provides the transformation matrix needed to go from the DTM reference frame (S-frame) to the Bennu principal-axis reference frame (P-frame) outlined in Equation (2):

It was known when analyzing the Recon B data set during operations that there exists a constant bias between the two OLA modes. Table 6 provides the estimated corrections or deltas to the HELT and LELT bias, per phase and combined. Per-phase estimates are reported in order to show the statistical consistency of the OD setup. Table 6 shows a statistical discrepancy between the estimated yaw, pitch, and roll parameters between Orbital A and Recon B as well as the LELT bias when compared to the combined solution. We believe that the differences and optimistic uncertainties are due to the insensitivities of the data in their orbital phases.

Using the OLA v21 DTM, the constant bias was determined to be 48.72 ± 1.46 cm in the HELT mode and 20.59 ± 1.73 cm the LELT mode. The difference between the HELT and LELT biases is 28.13 ± 2.26 cm (assuming uncorrelated values), which is within 1σ of the estimated difference of 25.85 ± 2.46 cm (assuming uncorrelated values) by Goossens et al. (2021). We see that the reconstructed trajectory for Orbital B and Recon B are biased radially by around 5 and 10 cm, respectively, when compared to the combined solution. The estimated trajectory in these cases is adjusted to compensate for the discrepancy in the Orbital B and Recon B LELT bias when compared to the combined solutions and adjusting the dynamics and GM accordingly to find a solution that is common to all of the data arcs.

We determined that a constant error in the boresight for both HELT and LELT was necessary. Goossens et al. (2021) does not estimate a correction to the OLA reference frames; however, a significant correction is necessary to accurately place the lidar intercept location on the model. The total angular difference in the boresight between the Orbital A and combined solution is about 6.0 mdeg, which equates to roughly 17 cm on the surface. For Recon B, this angular difference in the boresight is around 5.6 mdeg, which is roughly 7 cm on the surface. These constant corrections to the boresight help to achieve a better initial placement of the intercept points. In addition to this, the stochastic pointing corrections that are estimated per scan, as outlined in Table 4, have a 3σ variation of 14.4 mdeg for yaw, 6.8 mdeg for pitch, and 8.1 mdeg for roll in Orbital A and 12.9 mdeg for yaw, 5.1 mdeg for pitch and 6.8 mdeg for roll in Recon B. These random errors are due to thermal distortions on the instrument deck due to heating from OLA during the HELT and LELT modes along with other activities from science instruments and slewing to/from

$$[\boldsymbol{R}_{S}^{P}] = \begin{bmatrix} 9.999999029227679E-01, & 0.000000000000000E+00, & -4.406296117896816E-04 \\ -4.445187076223213E-08, & 9.999999949113483E-01, & -1.008826126469799E-04 \\ 4.406296095474709E-04, & 1.008826224403856E-04, & 9.999998978341166E-01 \end{bmatrix}. \tag{3}$$

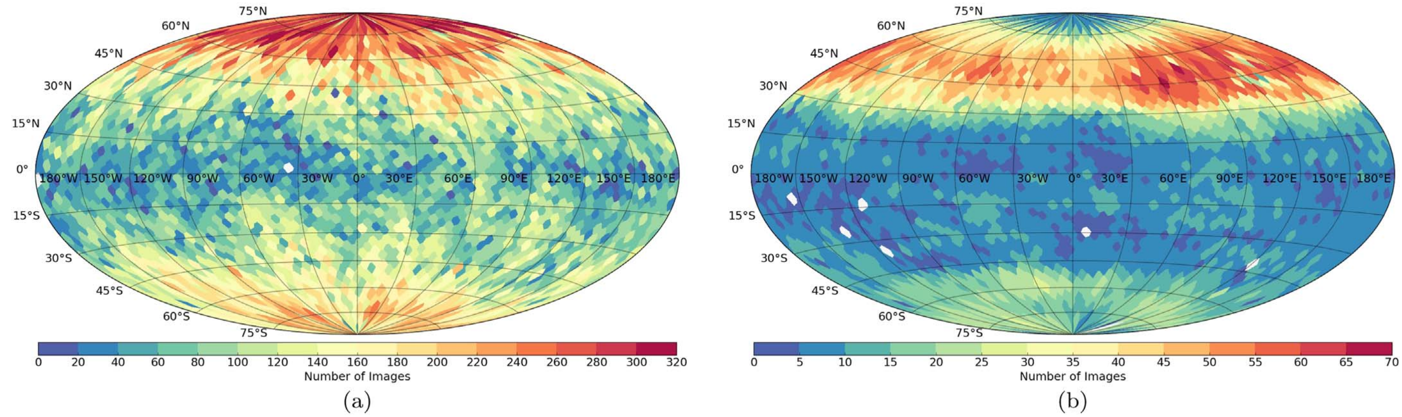

Figure 1. Number of images in this analysis that were correlated per landmark for NavCam 1 (a) and MapCam (b). Landmarks without any color were not correlated in a single image for the duration of data listed in Table 3.

Table 6
Estimation Corrections for OLA v21 DTM Lidar Parameters

	Estimated Parameter	Orbital A	Orbital B	Recon B	Combined
LELT	Bias (cm)	⋯	26.25 ± 0.95	29.36 ± 1.59	20.59 ± 1.73
	Yaw (mdeg)	⋯	−40.56 ± 3.27	−44.10 ± 1.18	−42.23 ± 2.32
	Pitch (mdeg)	⋯	20.97 ± 3.15	14.41 ± 0.73	16.59 ± 0.77
	Roll (mdeg)	⋯	−12.65 ± 3.15	−16.23 ± 0.74	−15.28 ± 0.77
HELT	Bias (cm)	46.80 ± 2.06	⋯	48.96 ± 1.59	48.72 ± 1.46
	Yaw (mdeg)	−41.03 ± 1.01	⋯	−30.35 ± 0.93	−39.73 ± 1.12
	Pitch (mdeg)	19.47 ± 0.86	⋯	9.66 ± 0.55	13.59 ± 0.51
	Roll (mdeg)	−1.04 ± 0.13	⋯	−6.67 ± 0.56	−2.17 ± 0.36

different attitudes. Equations (4) and (5) provide the transformation from the spacecraft reference frame (denoted *s/c*) to the OLA scanning mirror reference frame for HELT and LELT, respectively. The estimated corrections to the OLA reference frames from the operations kernel (Semenov & NAIF 2019) move the projection of the altimetry intercept points 30 cm for LELT and 46 cm for HELT, assuming a 750 m altitude:

$$[\boldsymbol{R}_{s/c}^{\mathrm{HELT}}] = \begin{bmatrix} 9.9999854833769 93E-01, & 7.271017095638325E-04, & -1.540988513244261E-03 \\ -7.257740606831637E-04, & 9.999993651548387E-01, & 8.619407939083507E-04 \\ 1.541614253579953E-03, & -8.608211331706713E-04, & 9.999984412050200E-01 \end{bmatrix}, \tag{4}$$

$$[\boldsymbol{R}_{s/c}^{\mathrm{LELT}}] = \begin{bmatrix} 9.999984972051222E-01, & 6.833465664034615E-04, & -1.593306300498007E-03 \\ -6.823386716339377E-04, & 9.999995668380216E-01, & 6.330384713338627E-04 \\ 1.593738195004085E-03, & -6.319503455023028E-04, & 9.999985303175833E-01 \end{bmatrix}. \tag{5}$$

Figure 2 provides the NavCam 1 OpNav landmark residuals from Orbital A in the pixel and line coordinates. During this phase, the camera was aligned such that the pixel coordinate was toward the Sun, and the line coordinate was along the terminator (downtrack in the spacecraft direction of motion). The residuals are plotted against emission angle, illumination angle, and the correlation score from the SPC cross-correlation of the image with the maplet. Noise level increases with emission angles. No significant trend in noise is apparent with respect to the illumination angle of the feature. There is a slight increase in noise at lower correlation scores.

The distribution of the landmark data is given in the histogram above the plots. The median emission angle for Orbital A was 35.83°, the median illumination angle was 62.35°, and the median correlation score was 0.498. The OLA

5.2. Landmark OpNav Performance

Figure 1 shows the total number of NavCam 1 and MapCam images with which each landmark of the OLA v21 DTM correlated over the analysis span shown in Table 3. Images used for this analysis correlated with landmarks globally across Bennu, with significant coverage of landmarks at the polar regions. Two landmarks were not correlated in the entire set of NavCam 1 data, and seven landmarks were not correlated in the MapCam data set.

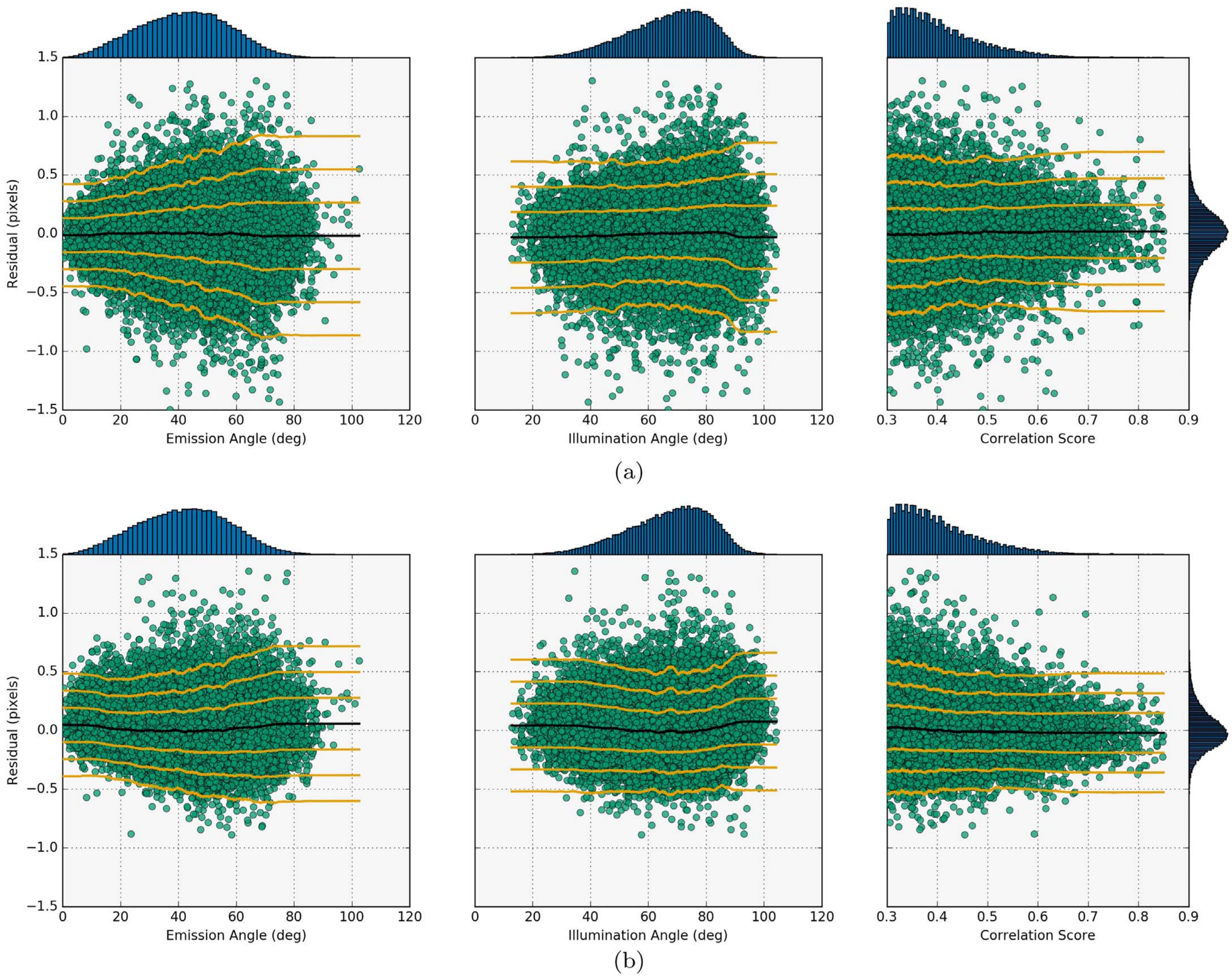

Figure 2. Orbital A landmark OpNav residuals in the camera pixel (a) and line (b) directions. The bluish green dots are the residuals, the black line is the mean of the residuals, and the orange lines indicate the 1, 2, and 3σ standard deviations around the mean. The residuals are plotted vs. the emission angle, the illumination angle, and the correlation score of the landmark. A histogram of the data distribution is provided for each plot in blue.

v21 DTM's smooth albedo typically provided lower correlation scores when compared to the SPC v42 DTM.

The NavCam 1 landmark OpNav statistics per phase are shown in Figure 3. Similar to Figure 2, the residuals statistics are plotted versus the emission angle, the illumination angle, and the correlation score of the landmark. The residuals are converted from pixels to centimeters by using the GSD of the landmarks in the image.

Figure 4 shows the per-phase standard deviation of the landmark residuals in centimeters at the surface. The magnitude of the pixel/line residual error is converted to centimeters using the GSD of the landmark at the image epoch and altitude. The standard deviation of the landmark is only provided for landmarks observed in more than five images during the mission phase analyzed in Table 3. Orbital A (Figure 4(a)), Orbital C (Figure 4(c)), and Orbital R (Figure 4(d)) had near-complete coverage of the surface of landmarks with more than five images. Orbital B (Figure 4(b)) had near-complete coverage of the landmarks, but a significant portion of low-latitude landmarks did not correlate in more than five images. Recon B (Figure 4(e)) had the least coverage globally, with a significant portion of the equatorial and midlatitude regions not having a single correlated image. From Orbital A and Orbital C data alone, the OpNav residual 1σ standard deviations show that a majority of the landmarks have a standard deviation less than 15 cm 1σ, consistent with the resolution of the OpNav DTMs of 15 cm. Orbital B and Orbital R provide more information on the quality of the DTMs, with a majority of the landmarks having a standard deviation of less than 7.5 cm 1σ.

5.3. Landmark Estimation

The combined OD solution using data from all phases analyzed in this work was used to evaluate the landmark locations provided by the OLA v21 DTM. The resolution of the landmark maplets was 15 cm GSD globally with 2500 maplets generated. The "landmark" of the maplet is simply the center of a 99 $\times$99 grid with 15 cm per grid spacing. The locations of all 2500 landmarks are estimated simultaneously to determine the accuracy of the landmark relative to the OD combined solution and the uncertainty associated with the landmark location

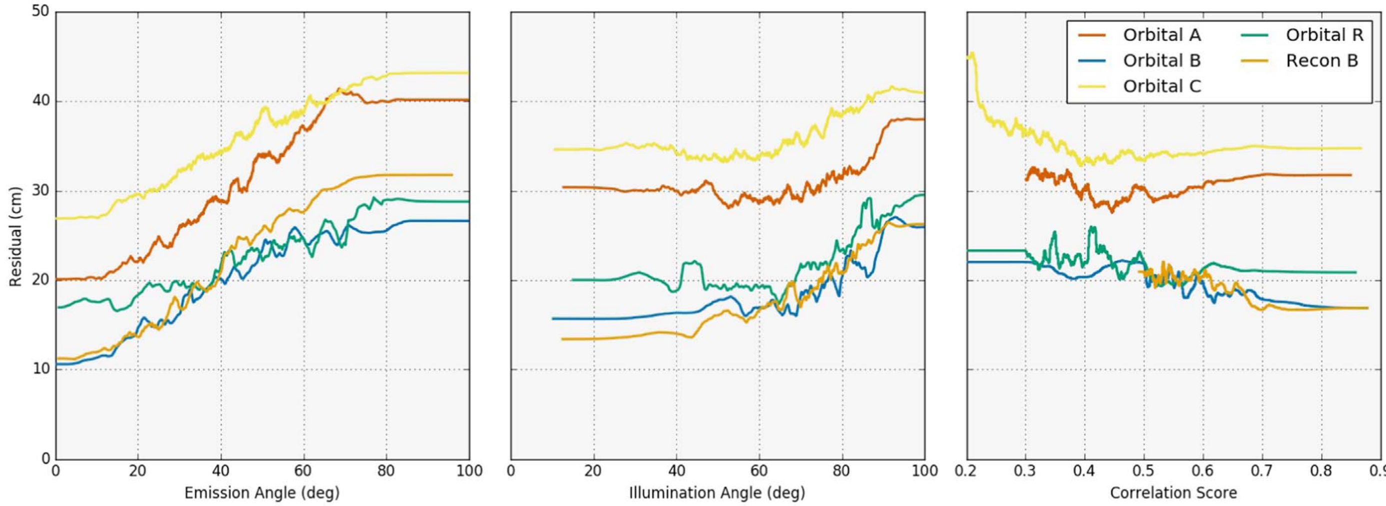

(a)

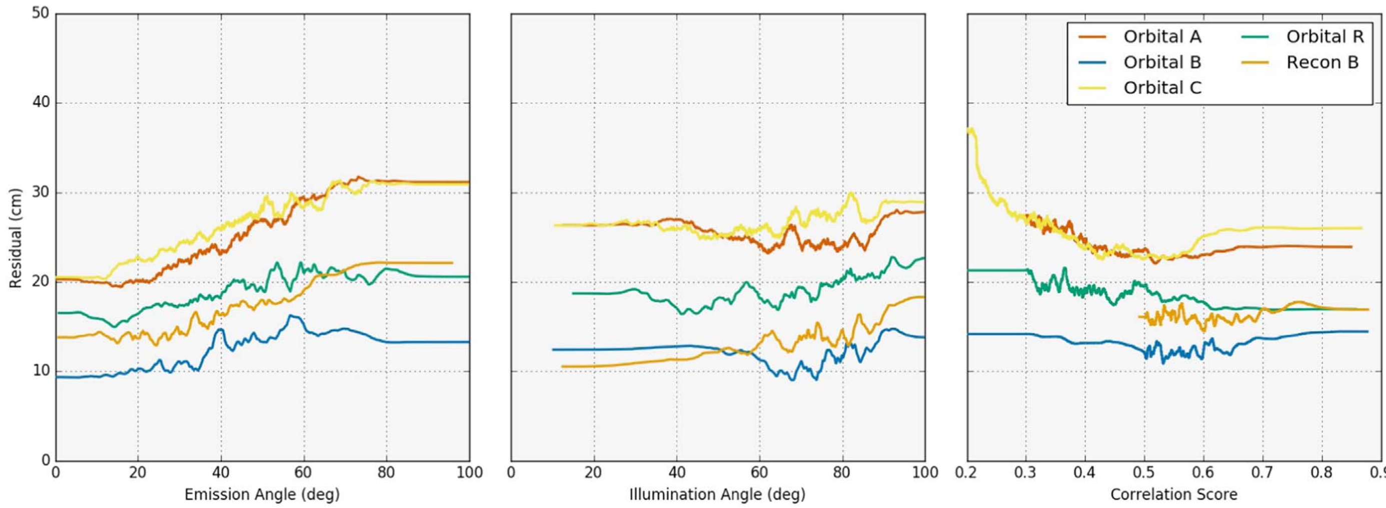

(b)

Figure 3. Landmark OpNav residual 3σ standard deviations per phase in the camera pixel (a) and line (b) directions. Residual 3σ standard deviations are plotted vs. the emission angle, the illumination angle, and the correlation score of the landmark.

estimate. The landmark estimation analysis performed assumes the solved for trajectories from the combined solution estimated in the previous sections and their associated parameter estimates. While the location estimate provides an idea of the accuracy and consistency of the maplet locations, the estimated a posteriori uncertainty in the landmark location gives insight into how much information is contained in the images to determine the landmark location.

The estimation of the OLA v21 landmark locations uses the COMCOF correction and DTM frame corrections given in Table 5. This was done to center the model on the center of mass of Bennu and orient the pole of the OLA v21 DTM with the principal-axis reference frame. By doing this, the estimated landmark corrections should not exhibit any systematic rotation along the surface or a mean offset in the location corrections. If a large mean offset in the location corrections is estimated, the COMCOF and DTM frame corrections would be updated and the landmark locations reestimated. Figure 5 provides the estimated corrections and uncertainties in the local landmark topographic east-north-zenith (ENZ) reference frame. In this reference frame, positive corrections are given in eastward, northward, and radially outward from the center of Bennu. The average eastward estimated correction of all the values in Figure 5(a) was determined to be -0.04 cm with an average uncertainty for Figure 5 of 4.96 cm 1σ. This small eastward correction indicates that no further modification to the prime meridian is necessary. Figures 5(c) and (d) provide the global northward corrections and uncertainties, respectively, which average -0.08 cm and 5.53 cm. These minimal corrections to landmark locations in the eastward and northward directions indicate that the model is oriented correctly with the values given in Table 5. Due to a mean subcentimeter shift in the landmark locations using the estimated COMCOF and DTM frame corrections given in Table 5, no additional iteration is necessary. Finally, the global radial corrections and uncertainties can be seen in Figures 5(e) and (f). The average radial correction is 7.65 cm with an average uncertainty of 5.96 cm 1σ. This average radial correction reduces the standard deviation of the NavCam residuals from 0.24 px 1σ to 0.19 px 1σ and that the OpNav data estimates the DTM to be 7.65 cm or roughly 0.031% larger, assuming a 245 m average radius for Bennu.

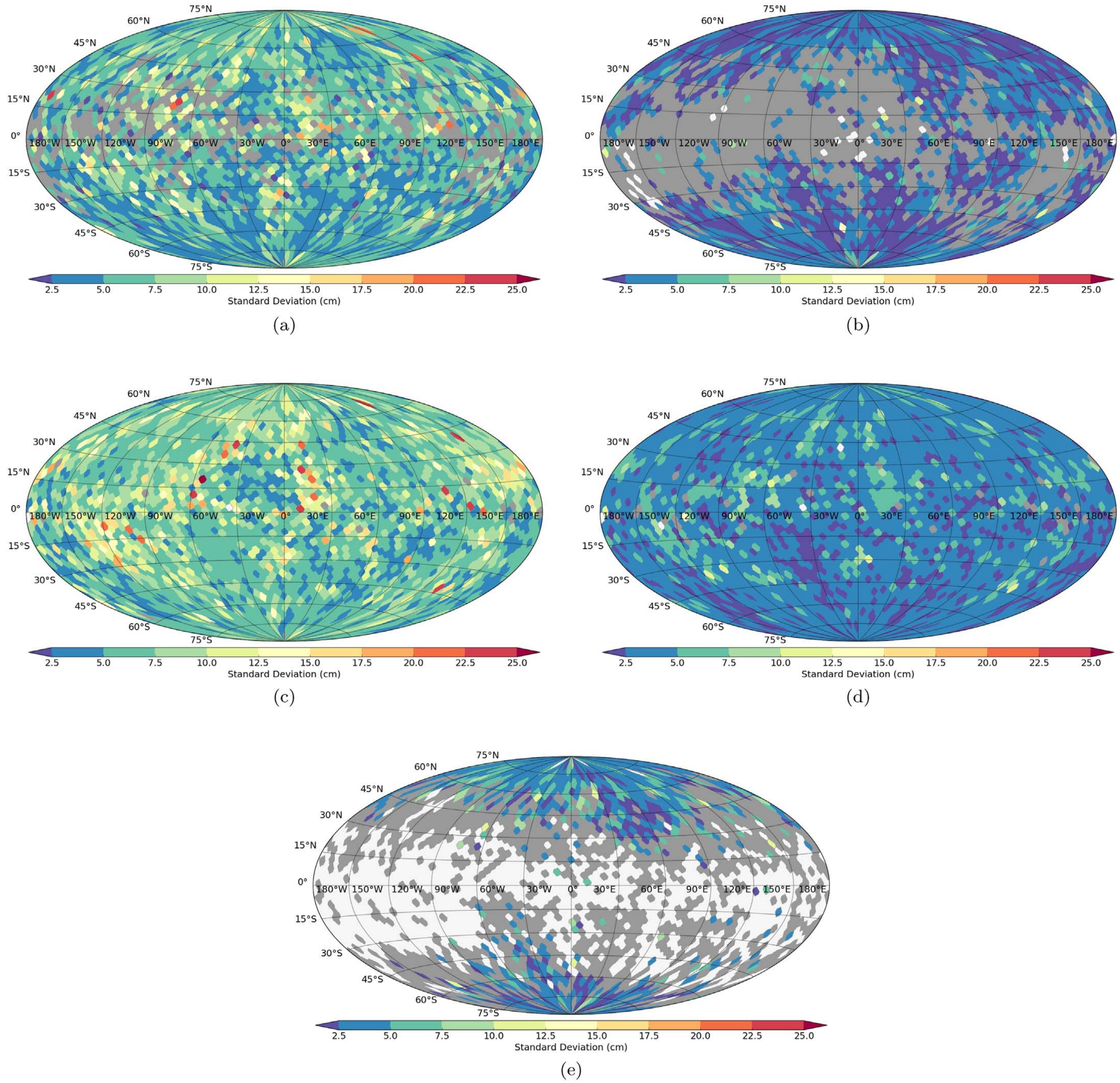

Figure 4. Standard deviation of OpNav residuals projected on the surface in centimeters per landmark for Orbital A (a), Orbital B (b), Orbital C (c), Orbital R (d), and Recon B (e). Gray indicates that there were fewer than five images of that landmark and no statistics were calculated. No color indicates that there were no images of that landmark.

Figures 6(a) through (c) show the signal-to-noise ratio (S/N) of the landmark corrections estimated. The S/N is defined as the absolute value of the estimated landmark correction divided by the estimated a posteriori uncertainties. A low S/N generally indicates low confidence in the estimated correction or a small deviation relative to the a posteriori uncertainties, while a high S/N indicates a high confidence in the estimate or a large correction relative to the a posteriori uncertainties. The mean S/N globally is 0.4 for the east/west direction, 0.5 for the north/south direction, and 1.6 for the altitude direction. Figure 6(c) shows that the confidence in the altitude correction is high near the poles and lower near the equator, with the global S/N of 1.6 indicating that the mean correction of 7.65 cm is still not statistically significant. The global low S/N in Figures 6(a) and (b) are indicative of the small estimated corrections. Figure 6(b) shows regional corrections near the poles having an S/N of 2–3, which correspond to the larger estimated corrections seen in Figure 5(c).

5.4. OLA Performance

The ray-traced precision of OLA data is one indication of how well the OLA v21 DTM matches the combined orbital data solution. Similarly, analyzing the errors in the projected

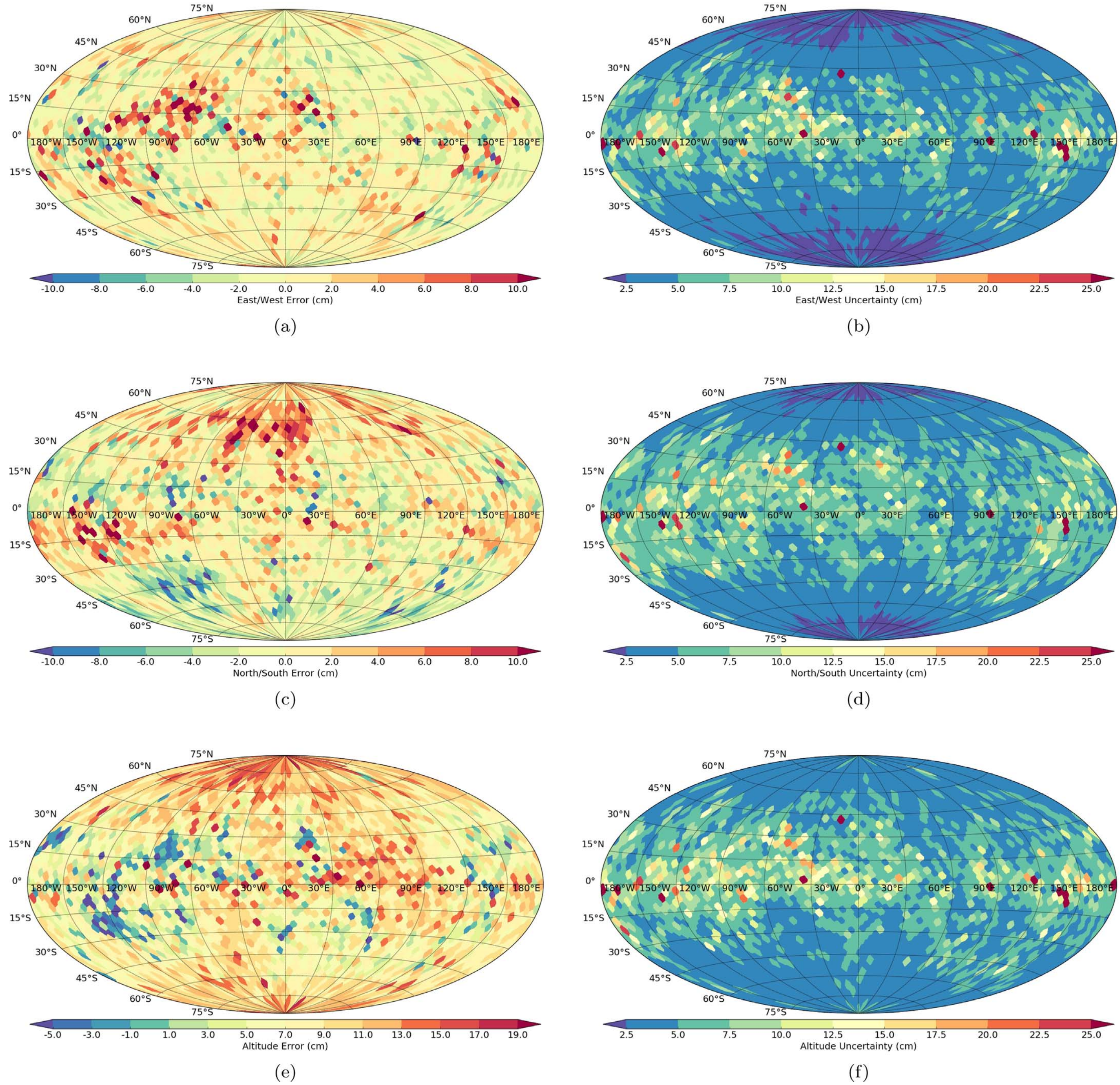

Figure 5. Estimated landmark location corrections and uncertainties for the combined solution. East/west (positive eastward) estimated deviations (a) and 1σ uncertainties (b). North/south (positive northward) estimated deviations (c) and 1σ uncertainties (d). Altitude (positive radially) estimated deviations (e) and 1σ uncertainties (f).

point clouds can give an indication of the fit quality of the lidar data with the OLA v21 DTM. The point clouds are projected onto the OLA v21 DTM using the best estimates of the OLA pointing corrections and biases obtained from the combined solution. A point-to-plane or point-to-point error metric is used to fit point-cloud data to the model. By adjusting the OLA instrument model and the translation and rotation offsets of the OLA v21 DTM using the estimates in Table 6, the precision of the instrument is revealed.

Figures 7 through 9 give the OLA ray-traced residual performance from the combined solution fit versus the off-nadir angle and the interior angle. The off-nadir angle is defined as the angle between nadir (lidar to Bennu vector) and the lidar direction at transmission. The interior angle (Iota) is the angle between the radial vector (Bennu to lidar vector) and the intercept location on the surface vector. Both angles are given to compare to the results given in Goossens et al. (2021) and to provide a different interpretation of the potential for a scale error in the DTM or spacecraft orbit error. As shown in Goossens et al. (2021), the off-nadir angle can give an idea of the bias, scale, and orbit errors. However, owing to variations from circular in the actual orbit, this metric is not consistent. We provide an alternative look at how the bias, scale, and orbit errors are mapped into a consistent location error using the

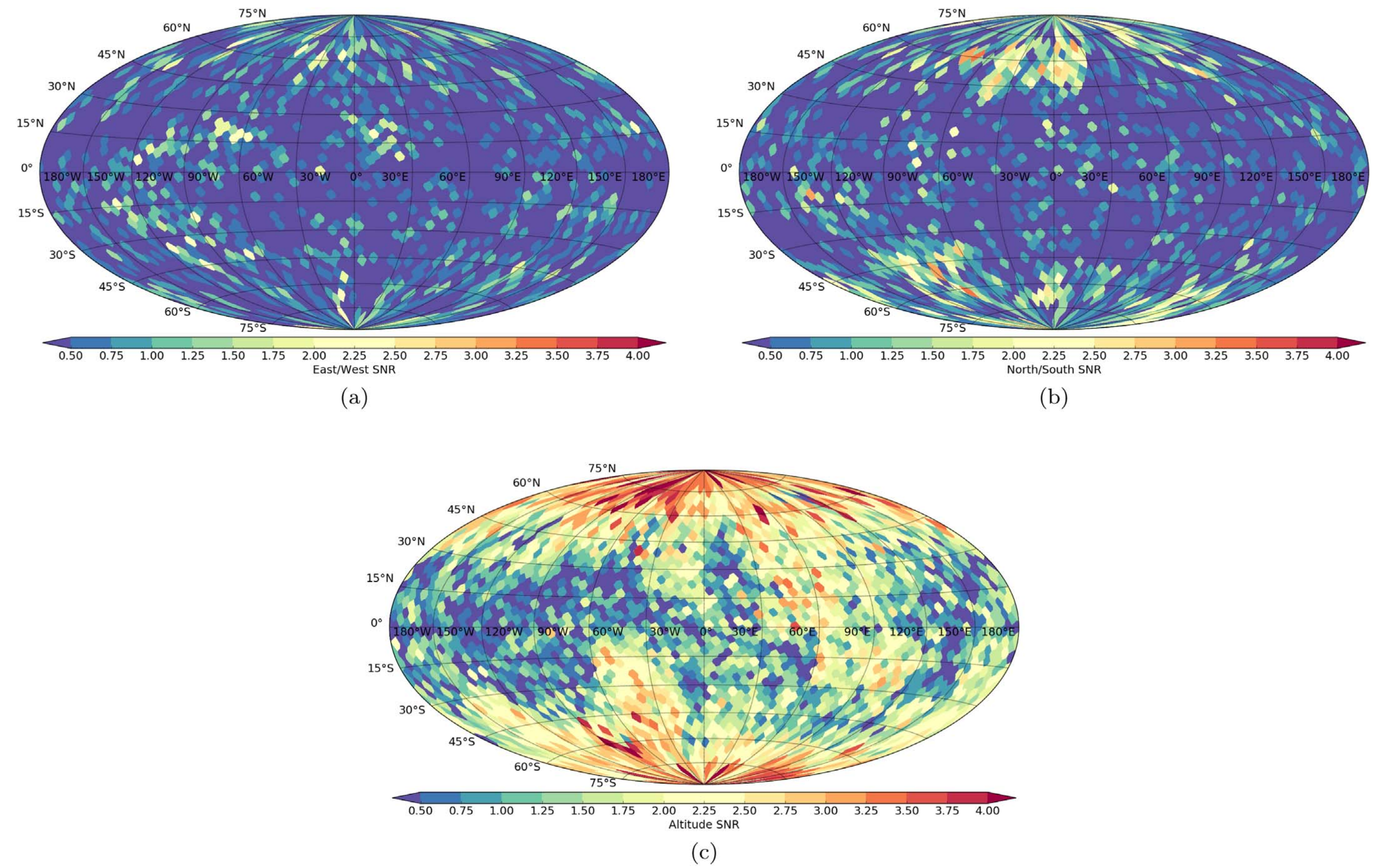

Figure 6. Estimated landmark location S/N for the combined solution. East/west (positive eastward) estimated S/N (a), North/south (positive northward) estimated S/N (b), and altitude (positive radially) estimated S/N (c).

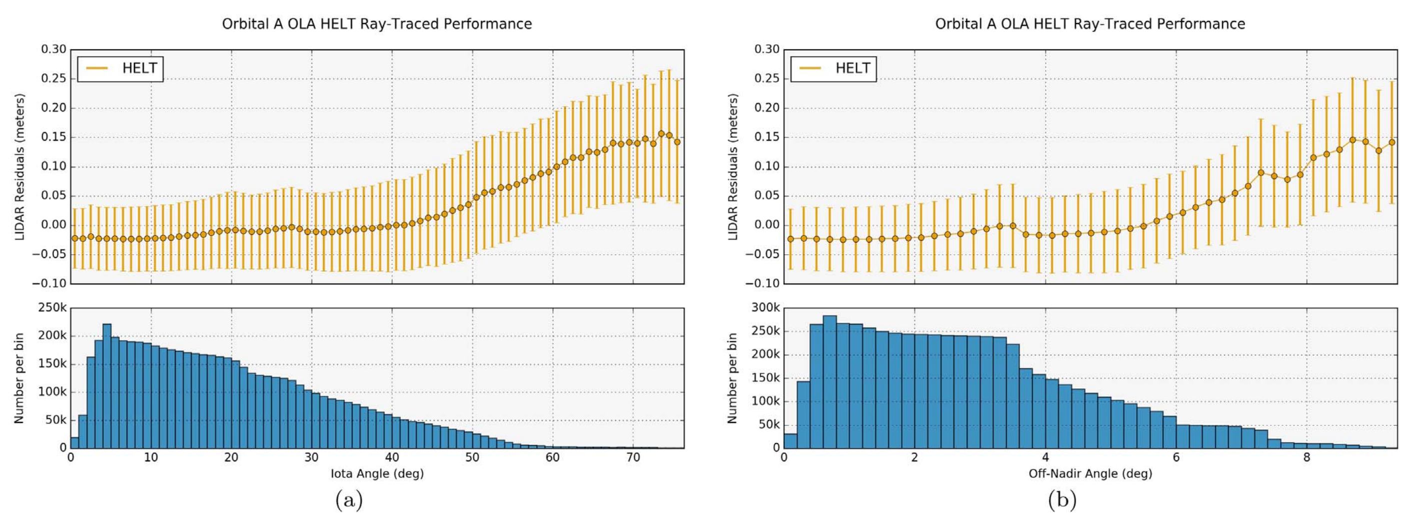

Figure 7. OLA performance for Orbital A vs. Iota (a) and the off-nadir angles (b). The HELT mean and 1σ standard deviation is given in orange. Histograms of the data per bin are given in blue.

interior angle (Iota) that is agnostic to variations in the orbit altitude.

The statistics (mean and 1σ standard deviation) given by the error bars in Figures 7 through 9 are computed by removing 6σ outliers after a minimum covariance determinant (Rousseeuw 1984; Rousseeuw & Driessen 1999; Hubert & Debruyne 2010) of the binned data is computed. The data are binned every 1° for Iota and every 0.2 deg for the off-nadir angle. The bottom portions of the subplot show the histogram of the data analyzed over the bin. The Orbital A data show a ranging precision of 5 cm 1σ at nadir, which grow to 10 cm 1σ near the limb of the scans (Figure 7). Orbital B has the least structure in the data at various angles with a nadir ranging precision of 3 cm 1σ growing to 4 cm 1σ for larger angles (Figure 8). In Recon B, the only phase that had measurements in both the HELT and LELT modes, the difference between the

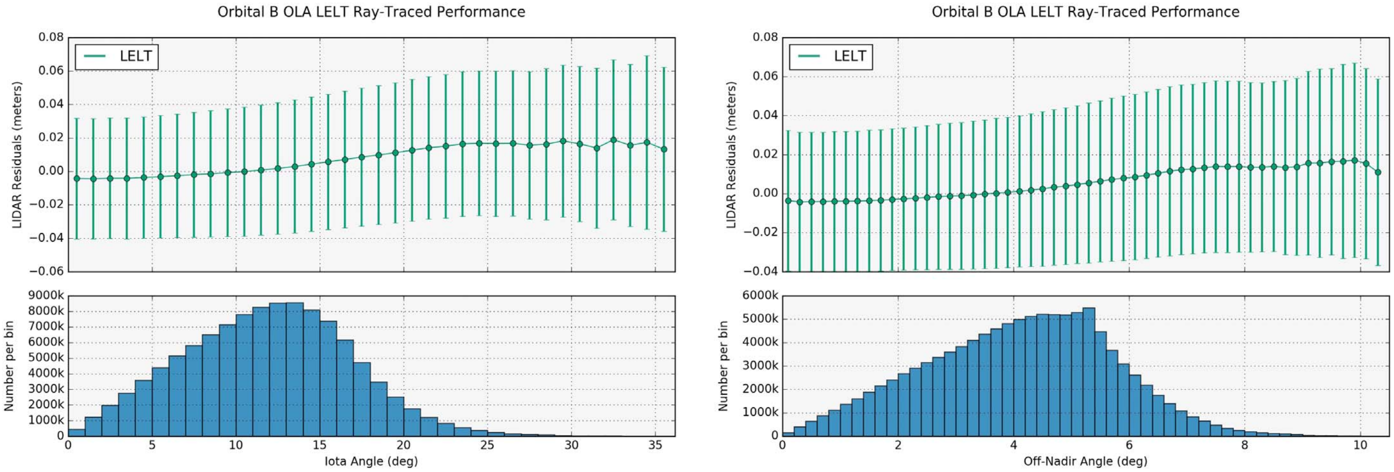

(a) (b)

Figure 8. OLA performance for Orbital B (a, b) vs. Iota (a) and the off-nadir angles (b). The LELT mean and 1σ standard deviation is given in green. Histograms of the data per bin are given in blue.

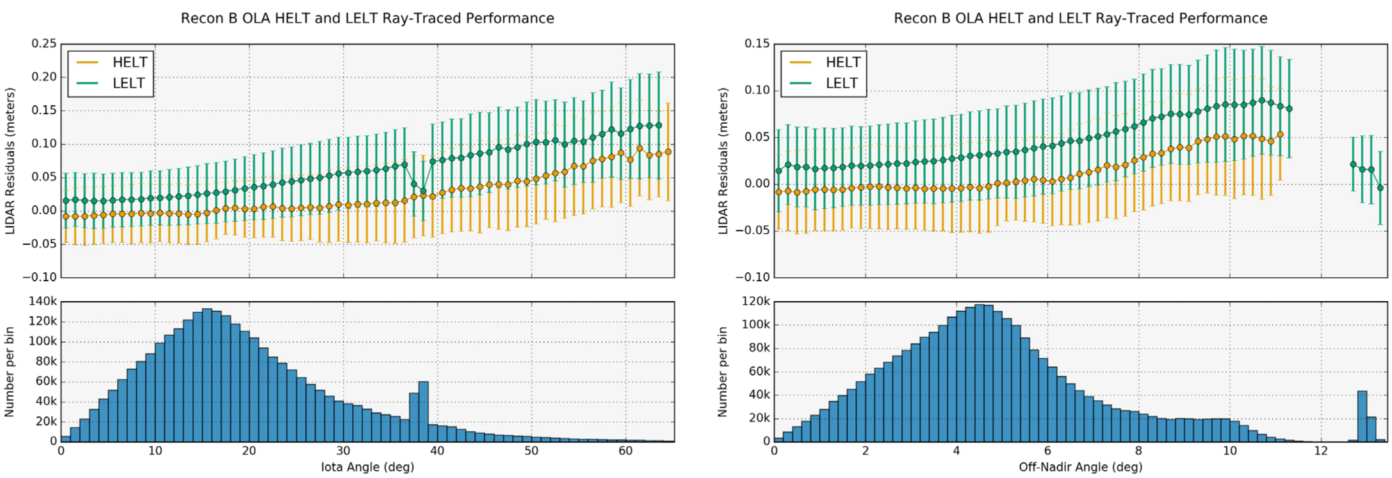

(a) (b)

Figure 9. OLA performance for Recon B (a, b) vs. Iota (a) and the off-nadir angles (b). The HELT mean and 1σ standard deviation is given in orange, while the LELT performance is given in green. Histograms of the data per bin are given in blue.

Table 7
OLA Statistics per Phase and in the Combined Solution

	Ray-traced			Point-to-Plane		
Phase	*N* Points	Mean (cm)	Standard Deviation (cm)	*N* Points	Mean (cm)	Standard Deviation (cm)
Orbital A	5,928,203	−0.10	10.56	7,667,932	−0.85	6.05
Orbital B	108,866,584	0.40	6.77	229,681,844	−0.18	3.64
Recon B	5,755,960	2.01	8.65	6,072,939	0.81	4.85
Combined	120,550,747	0.41	7.12	243,422,715	−0.18	3.78

means of the data versus the iota or off-nadir angle shows a slight error of 2 to 3 cm (Figure 9). The noise is greater than that seen in Orbital B of 4 cm 1σ at nadir up to 7 cm 1σ at the extreme angles.

The overall ray-traced and point-cloud performance of the OLA v21 DTM is given in Table 7 for each phase and in combination. The ray-traced data were decimated from the original data using every 20th OLA return, whereas the point-cloud data were decimated every 10th OLA return. A minimum covariance determinant was used to remove the outliers of the data for each of the phases. The number of points processed, means, and standard deviations of the OLA data are provided. The Orbital B data set has the best fitting residuals for the ray-traced model and the point-to-plane error metric.

When comparing the ray-traced performance to the values given in Goossens et al. (2021), we see an improvement. The performance values provided in Goossens et al. (2021) are given as a mean and rms, which are converted here to standard deviations for consistency in the comparisons. For Orbital B, the OLA residuals mean and standard deviation are reduced

Table 8
Estimation Results for Scaled OLA v21 DTM Lidar Parameters

	Estimated Parameter	Orbital A	Orbital B	Recon B	Combined
LELT	Bias (cm)	⋯	-3.26 ± 3.79	1.33 ± 4.53	-1.54 ± 3.47
	Yaw (mdeg)	⋯	-40.73 ± 3.07	-35.08 ± 5.30	-42.41 ± 2.86
	Pitch (mdeg)	⋯	19.92 ± 2.97	14.82 ± 2.93	16.47 ± 0.84
	Roll (mdeg)	⋯	-13.34 ± 2.88	-15.20 ± 2.92	-15.37 ± 0.85
HELT	Bias (cm)	14.00 ± 3.84	⋯	22.35 ± 4.48	19.43 ± 3.63
	Yaw (mdeg)	-41.12 ± 1.28	⋯	-28.84 ± 4.73	-42.43 ± 1.19
	Pitch (mdeg)	19.09 ± 0.88	⋯	10.07 ± 2.92	13.34 ± 0.54
	Roll (mdeg)	-1.10 ± 0.24	⋯	-5.82 ± 2.91	-2.16 ± 0.36

from -0.22 ± 21.1 cm (Goossens et al. 2021) to 0.40 ± 6.77 cm. Similarly, for Recon B, the OLA residuals mean and standard deviation are reduced from 3.55 ± 18.2 cm to 2.01 ± 8.65 cm. This improvement in the data fit is most likely due to a combination of a higher-resolution DTM: Goossens et al. (2021) used an internally generated 20 cm resolution map based on the OLA v20 DTM (Daly et al. 2020), whereas we use the 5 cm resolution triangular mesh directly, correcting the orientation of the OLA HELT and LELT modes, and improved measurement weighting.

5.5. Comparing DTM Navigation Requirements with Performance

Prior to ProxOps, the navigation requirements levied on the accuracy of the SPC DTMs used for navigation were related to the resolution of the landmark maplets and the overall performance of the OpNav residuals. There were no requirements levied on the accuracy of the OLA DTMs for use in navigation-related products as the OLA data were never baselined as a navigation observable to be processed during the mission.

The pre-ProxOps navigation analysis that all mission-related requirements were based off of assumed an OpNav weighting algorithm related to the DTM GSD and the distance between the spacecraft to the landmark (Antreasian et al. 2016; Leonard et al. 2020a; Adam et al. 2022a). For the Orbital A phase, a global set of 75 cm GSD DTM was assumed to be available from SPC DTMs constructed during the Preliminary Survey phase and a 35 cm GSD DTM was assumed for Orbital B and later. The OpNav data performance of the model was assumed to be captured by the weighting scheme:

$$W = (W_{\min}^2 + (S/R)^2)^{1/2}, \tag{6}$$

where W is the expected landmark noise in the pixel or line direction, $W_{\min}$ is the minimum weighting (assumed to be 1.0 for the analysis), S is the shape model GSD, and R is the camera resolution of the landmark. The camera resolution is related to the instantaneous field-of-view (iFOV), and r, the distance to the landmark from the camera, such that $R = r \times i\mathrm{FOV}$. The landmark residual noise for NavCam was expected to range between 1.6 and 2.1 px (1σ) for a 75 cm shape model for Orbital A and between 1.9 and 3.0 px (1σ) for a 35 cm shape model for Orbital B. The performance observed using the OLA v21 DTM was 0.24 px (1σ) for Orbital A and 0.27 px (1σ) for Orbital B, significantly better than the requirements used for navigation analysis prior to ProxOps.

During ProxOps a global DTM scale discrepancy of 1 m was identified between the SPC- and OLA-based DTMs. This level of error exceeded the 14 cm global accuracy requirement for the onboard DTMs used to navigate the spacecraft to the surface with natural feature tracking (NFT; Norman et al. 2022; Olds et al. 2022) Estimation of the landmark locations was used to validate the final shifts that were used to align the SPC v42 DTMs to the OLA v20 DTMs. The analysis performed in Section 5.3 is the same as what was performed during operations to evaluate the TAG DTM and NFT DTMs used for navigation. We find that 7.5% (188/2500) of the estimated landmark corrections (188/2500) do not meet this 14 cm total shift and 2.8% (69/2500) have an S/N greater than 2. When removing the 7.65 cm radial bias from estimated landmark correction, we find that 2.3% (57/2500) of the estimated landmark corrections (5/2500) do not meet this 14 cm total shift and 0.2% (5/2500) have an S/N greater than 2. During ProxOps, the GNC team tested DTM location errors as large as 30 cm and found that the navigation performance was still acceptable for the NFT system performance. We find that none of the estimated landmark corrections exceed this 30 cm error.

Since no requirements existed for OLA performance concerning navigation analysis, we can only compare the performance seen in our analysis with the performance requirements given in Table 2. The OLA performance shown in Figures 7 through 9 and Table 7 meet the range precision requirements given in Table 2. The estimated LELT and HELT biases given in Table 6 of 20.59 and 48.72 cm, respectively, also fall within the performance requirements of Table 2 for the range accuracy.

6. Results with Shape Model Scale Factor Estimation

With the final on-orbit OLA mirror calibration provided by Seabrook et al. (2022) showing that the mirror scaling was originally in error, the concern still remains that an overall scaling issue may exist in the mirror azimuth and elevation coordinates. Goossens et al. (2021) estimates that the overall scale of the model could be in error by 1.000896 ± 0.00036. Seabrook et al. (2022) provides a detailed explanation of the calibration of the mirror scaling and justification for the estimates through the use of image-to-OLA keypoint maplet comparisons. If there does exist an overall scale factor to the model, the following analysis attempts to estimate it by adjusting the DTM and SPC maplet scales in tandem to provide a consistent estimate between phases and the combined solution of all the phases of data. No corrections to the landmark locations that were estimated in Section 5.3 were applied in the following analysis.

Table 9
Estimation Results for Scaled OLA v21 DTM Reference Frame Translation and Rotation Offset

Estimated Parameter	Orbital A	Orbital B	Orbital C	Orbital R	Recon B	Combined
Scale	+0.042% ± 0.002%	+0.056% ± 0.006%	+0.088% ± 0.005%	+0.083% ± 0.005%	+0.052% ± 0.004%	+0.049% ± 0.005%
$\boldsymbol{r}_{CF}^{P}$ X (cm)	5.21 ± 0.22	4.71 ± 0.09	4.60 ± 0.40	4.77 ± 0.11	5.04 ± 0.29	4.81 ± 0.07
$\boldsymbol{r}_{CF}^{P}$ Y (cm)	−3.45 ± 0.22	−3.03 ± 0.09	−3.35 ± 0.41	−2.89 ± 0.11	−3.04 ± 0.29	−3.14 ± 0.07
$\boldsymbol{r}_{CF}^{P}$ Z (cm)	0.35 ± 2.28	7.78 ± 0.40	15.98 ± 4.54	−2.90 ± 5.82	10.30 ± 1.11	7.50 ± 0.50
Pitch (mdeg)	24.57 ± 0.51	24.61 ± 0.25	24.50 ± 1.14	25.38 ± 0.32	24.30 ± 0.83	25.24 ± 0.18
Roll (mdeg)	−6.84 ± 0.50	-5.64 ± 0.26	−5.51 ± 1.13	−5.49 ± 0.31	−5.56 ± 0.78	−5.64 ± 0.17

Similarly to the results presented in Table 6, the estimated corrections to the OLA parameters are given in Table 8. The combined solution LELT yaw, pitch, and roll parameters in Table 8 are estimated to be statistically consistent by 0.06σ, 0.14σ, and 0.11σ from those reported in Table 6. The combined solution HELT yaw, pitch, and roll parameters in Table 8 are estimated to be statistically consistent by 2.27σ, 0.46σ, and 0.03σ from those reported in Table 6. The combined solution bias estimates for the HELT and LELT in Table 8 are smaller than those estimated in Table 6 because the overall OLA shape model scale factor has been applied. When at nadir point, the shape model scale factor and the OLA bias are directly correlated; they are weakly correlated for increasingly off-nadir angles.

Table 9 provides the estimated corrections for the overall shape model scale factor, as well as the COMCOF and pitch and roll corrections to the [$\boldsymbol{R}_S^P$] transformation. The results contain the same estimated parameters as those presented in Table 5, with the addition of the shape model scale factor estimates for each phase and the combined solution. The best estimate of the shape model scale factor for the combined solution is 1.00049 ± 0.00005. This estimate is within 1.1σ of the estimated value and uncertainty provided by Goossens et al. (2021). When performing this analysis, we noticed that the OpNav data were the primary source of information on the adjustment of the shape model scale factor, whereas the OLA data provided information mostly on the bias and not the scale factor. When estimating separate shape model scale factors for the DTMs used with OpNav data versus those used with OLA data, the OpNav data tended to scale the landmark maplet DTMs larger, consistent with the combined solution of 0.049%, whereas the OLA data estimated nearly no significant scale factor correction to the DTM. This disparity in the information content of each data type relative to the shape model scale factor showed that the OLA data were at odds with the image data.

7. Conclusions

The OLA v21 DTM is the most accurate and detailed terrain model of the asteroid Bennu based on extensive mapping and analysis of data collected during the OSIRIS-REx mission. A consistent data set from this model of 15 cm GSD maplets for image data and the 5 cm GSD DTMs for OLA measurements, combined with radiometric data, was used to estimate a global combined solution to the spacecraft trajectory and OLA v21 DTM. Data were used from five of the main orbital phases of the mission to produce individual and combined estimates of the corrections needed to align the OLA v21 DTM and parameters governing the OLA instruments HELT and LELT modes.

Utilizing this extensive data set, our results show that the OLA v21 DTM performs exceptionally well for the analyzed mission phases, producing consistent results. The estimated COMCOF for the OLA v21 DTM is on the order of a few centimeters, the result of iterations between the flight dynamics system and AltWG throughout the mission. There does exist a frame correction necessary to align the OLA v21 DTM into the principal-axis reference frame as given in Equation (3). Similarly, a constant rotational offset in the HELT and LELT modes was estimated and given by Equations (4) and (5), respectively. These frame offsets are necessary to project the OLA data accurately onto the surface. A constant bias was estimated for the HELT at 48.72 cm ± 1.46 cm and for the LELT at 20.59 cm ± 1.73 cm.

With these corrections to the OLA v21 DTM and OLA instrument, the altimeter data has a ray-traced residual performance of 0.41 ± 7.12 cm and a point-to-plane performance of −0.18 ± 3.78 cm. These values are significantly improved upon from the modeling given in Goossens et al. (2021), which provides the performance (given as rms but converted to standard deviations for consistency in comparison) of the HELT during Recon B as 7.79 ± 19.7 cm and the LELT during Orbital B as −0.22 ± 21.1 cm and Recon B as 1.48 ± 16.9 cm.

The OLA v21 DTM terrain was determined from altimeter data only and with minimal assessment done to compare it to image data. This work utilizes an extensive image library from NavCam 1 and MapCam to determine the quality of the DTM for use in landmark navigation. A correlation between noise with respect to emission angle and altitude was observed when comparing the landmark residuals between phases. No significant dependence on illumination angle was detected. A slight increase in the noise of the landmark data was detected at lower correlation scores but was relatively constant for a majority of the data analyzed. Estimates of the landmark locations exhibited no deterministic trends in the corrections for the east/west or north/south errors. The image data indicates an average 7.65 cm altitude error for the landmark set. The OpNav data set also provides an average estimated uncertainty in the landmark location of 4.96 cm east/west, 5.53 cm north/south (positive northward), and 5.96 cm in altitude (positive radially outward), globally.

Additionally, we provide solutions for the OLA v21 DTM and OLA instrument assuming that the global DTM scale is incorrect. Our estimate for the DTM scale factor is within 1.1σ of the estimated value and uncertainty given in Goossens et al. (2021). Initial analysis indicated that the optical image data drove the necessity for the estimation of the DTM scale factor when decoupled from the model used to process the OLA data.

A discrepancy between the optical and altimeter data still exists in which the optical data tend to indicate a scale factor that produces a larger global DTM. The estimates provided in this work are statistically consistent with those estimated by Goossens et al. (2021) but suggest a smaller correction on the order of 12 cm instead of 25 cm radially. If the scale increase from the image data is to be believed, additional effort must be made to accurately calibrate the OLA mirror and its inherent biases to produce a globally larger DTM. Seabrook et al. (2022) provides detailed analysis on the updated calibration, which greatly improved the consistency of the altimeter data with the image data. Currently, the landmark OpNav data set is the only data source suggesting that a globally larger DTM is necessary. This work shows that the OLA v21 DTM performs exceptionally well for the navigation purposes analyzed.

Acknowledgments

The authors acknowledge members of the OSIRIS-REx team including the Altimetry Working Group, orbit determination team, trajectory and maneuver design team, optical navigation team, and the Lockheed Martin flight operations team.

This material is based upon work supported by NASA under Contracts NNM10AA11C and NNG13FC02C. OSIRIS-REx is the third mission in NASA's New Frontiers Program. Dante Lauretta of the University of Arizona, Tucson, is the principal investigator, and the University of Arizona also leads the science team and the science observation planning and data processing. Lockheed Martin Space Systems in Denver built the spacecraft and is providing flight operations. Goddard Space Flight Center and KinetX Aerospace are responsible for navigating the OSIRIS-REx spacecraft. The development of OLA and Canadian science support were provided by a contract with the Canadian Space Agency.

Data Availability

All images and altimetric data from the OSIRIS-REx mission are available via the Planetary Data System at https://arcnav.psi.edu/urn:nasa:pds:context:investigation:mission.orex. The SPC v42 and OLA v21 DTMs are available by downloading the Small Body Mapping Tool at sbmt.jhuapl.edu.

ORCID iDs

Jason M. Leonard https://orcid.org/0000-0003-3632-6793
Jeroen L. Geeraert https://orcid.org/0000-0001-5377-4745
Leilah K. McCarthy https://orcid.org/0000-0003-3585-4754
Coralie D. Adam https://orcid.org/0000-0002-5795-2446
Peter G. Antreasian https://orcid.org/0000-0001-9040-310X
Olivier S. Barnouin https://orcid.org/0000-0002-3578-7750
Michael G. Daly https://orcid.org/0000-0002-3733-2530
Jeffrey A. Seabrook https://orcid.org/0000-0002-2163-7276
Dante S. Lauretta https://orcid.org/0000-0002-2597-5950

References

Adam, C. D., McCarthy, L. K., Leonard, J. M., et al. 2022a, PSJ, in press
Adam, C. D., Knutson, S., Billett, O., et al. 2022b, in AIAA SciTech Forum 2022 (Reston, VA: AIAA) AIAA 2022-1569
Al Asad, M., Philpott, L., Johnson, C., et al. 2021, PSJ, 2, 82
Antreasian, P., Adam, C., Leonard, J., et al. 2022, in AIAA SciTech Forum 2022 (Reston, VA: AIAA) AIAA 2022-2470
Antreasian, P., Bordi, J., Criddle, K., et al. 2005, in AAS/AIAA Astrodynamics Specialist Conf. (Lake Tahoe, CA) AAS 05–312
Antreasian, P., Leonard, J., McAdams, J., et al. 2018, in 41st Annual AAS Guidance, Navigation, and Control Conf. (Lake Tahoe, CA) AAS 18–062
Antreasian, P., Moreau, M., Jackman, C., et al. 2016, in Annual AAS Guidance, Navigation, and Control Conf. (Breckenridge, CO) AAS 16–101
Antreasian, P. G., Moreau, M. C., Adam, C. D., et al. 2019, in 42nd Annual AAS Guidance and Control Conf. (Breckenridge, CO) AAS 19–035
Barnouin, O., Daly, M., Palmer, E., et al. 2020, P&SS, 180, 104764
Barnouin, O. S., Daly, M. G., Palmer, E. E., et al. 2019, NatGe, 12, 247
Bos, B., Nelson, D., Pelgrift, J., et al. 2020, SSRv, 216, 71
Bos, B., Ravine, M., Caplinger, M., et al. 2018, SSRv, 214, 37
Broschart, S., Bhaskaran, S., Bellerose, J., et al. 2017, in 26th Int. Symp. on Space Flight Dynamics ISSFD, ISSFD–2017–096
Chesley, S. R., French, A. S., Davis, A. B., et al. 2020, JGRE, 125, e2019JE006363
Church, E., Bourbeau, T., Curriden, J., et al. 2020, in 43rd Annual AAS Guidance and Control Conf. (Breckenridge, CO) AAS 20–148
Daly, M. G., Barnouin, O. S., Dickinson, C., et al. 2017, SSRv, 212, 899
Daly, M. G., Barnouin, O. S., Seabrook, J. A., et al. 2020, SciA, 6 eabd3649
de Santayana, R. P., & Lauer, M. 2015, in Proc. of the 25th Int. Symp. on Space Flight Dynamics (ISSFD) (Munich)
Farnocchia, D., Chesley, S. R., Takahashi, Y., et al. 2021, Icar, 369, 114594
French, A., Leonard, J., Geeraert, J., et al. 2019, in AAS/AIAA Astrodynamics Specialist Conf. (Portland, ME) AAS 19-738
Gaskell, R. W., Barnouin, O. S., Daly, M. G., et al. 2022, PSJ, 4, 63
Gaskell, R. W. 2001, in AAS/AIAA Astrodynamics Specialists Conf. (Quebec City, Canada) AAS 01–422
Gaskell, R. W. 2002, in AAS/AIAA Astrodynamics Specialists Conf. (Breckenridge, CO) AAS 02–021
Gaskell, R. W. 2011, in AAS/AIAA Spaceflight Mechanics Meeting (New Orleans, LA) AAS 11–220
Gates, C. R. 1963, A Simplified Model of Midcourse Maneuver Execution Errors Technical Report No. 32-504, JPL, Caltech, https://ntrs.nasa.gov/api/citations/19640003365/downloads/19640003365.pdf
Godard, B., Budnik, F., Bellei, G., Muñoz, P., & Morley, T. 2017, in Int. Symp. on Space Flight Dynamics-26th ISSFD (Matsuyama, Japan) ISTS–2017–d–095/ISSFD–2017–095, https://issfd.org/ISSFD_2017/paper/ISTS-2017-d-095__ISSFD-2017-095.pdf
Godard, B., Budnik, F., Muñoz, P., Morley, T., & Janarthanan, V. 2015, in Proc. 25th Int. Symp. on Space Flight Dynamics–25th ISSFD (Munich), https://issfd.org/2015/files/downloads/papers/124_Godard.pdf
Golish, D., Drouet d'Aubigny, C., Rizk, B., et al. 2020, SSRv, 216, 12
Goossens, S., Rowlands, D. D., Mazarico, E., et al. 2021, PSJ, 2, 219
Guinn, J. R., & Wolff, P. J. 1993, in AAS/AIAA Astrodynamics Specialists Conf. (Victoria, British Columbia, Canada) 143, AAS 93–573
Hergenrother, C., Maleszewski, C., Li, J.-Y., et al. 2020, JGRE, 125, e2020JE006381
Hubert, M., & Debruyne, M. 2010, WIREs Comp. Stat., 2, 36
Lauretta, D., Adam, C., Allen, A., et al. 2022, Sci, 377, 285
Lauretta, D., Balram-Knutson, S., Beshore, E., et al. 2017, SSRv, 212, 925
Lauretta, D., Hergenrother, C., Chesley, S., et al. 2019a, Sci, 366, eaay3544
Lauretta, D. S., DellaGiustina, D. N., Bennett, C. A., et al. 2019b, Natur, 568, 55
Lauretta, D. S., Enos, H. L., Polit, A. T., Roper, H. L., & Wolner, C. W. 2021, in Sample Return Missions: The Last Frontier of Solar System Exploration, ed. A. Longobardo (Amsterdam: Elsevier), 163
Leonard, J., Moreau, M., Antreasian, P., et al. 2022, in 45th Annual AAS Guidance and Control Conf. (Breckenridge, CO) AAS 22–166
Leonard, J. M., Adam, C. D., Pelgrift, J. Y., et al. 2020b, E&SS, 7, e2019EA000937
Leonard, J. M., Antreasian, P. G., Jackman, C. D., et al. 2017, in Int. ESA Conf. on Guidance, Navigation, and Control Systems (Salzburg)
Leonard, J. M., Geeraert, J., Page, B., et al. 2019, in AAS/AIAA Astrodynamics Specialist Conf. (Portland, ME) AAS 19–714
Leonard, J. M., Geeraert, J. L., Page, B. R., et al. 2020a, in 43rd Annual AAS Guidance and Control Conf. (Breckenridge, CO) AAS 20–153
Mazarico, E., Goossens, S., Rowlands, D. D., et al. 2019, AGUFM, P53C–3458
Mazarico, E., Neumann, G., Rowlands, D., & Smith, D. 2010, JGeod, 84, 343
McCarthy, L. K., Adam, C. D., Nelson, D. S., et al. 2022, in 32nd AIAA/AAS Space Flight Mechanics Meeting (San Diego, CA)
McElrath, T., Watkins, M., Portock, B., et al. 2004, in AIAA/AAS Astrodynamics Specialist Conf. and Exhibit (Providence, RI) AIAA 2004–4982

Moyer, T. D. 2005, Formulation for Observed and Computed Values of Deep Space Network Data Types for Navigation, Vol. 3 (New York: Wiley)
Muñoz, P., Budnik, F., Godard, B., et al. 2012, in 23rd Int. Symp. on Space Flight Dynamics (Pasadena, CA)
Norman, C., Miller, C., Olds, R., et al. 2022, PSJ, 3, 101
Olds, R., Miller, C., Norman, C., et al. 2022, PSJ, 3, 100
Owen, W. M., Jr 2011, in AAS Spaceflight Mechanics Conf. (New Orleans, LA) AAS 11–215
Palmer, E. E., Gaskell, R., Daly, M. G., et al. 2022, PSJ, 3, 102
Pelgrift, J. Y., Lessac-Chenen, E. J., Adam, C. D., et al. 2020, E&SS, 7, e2019EA000938
Pelgrift, J. Y., Sahr, E. M., Nelson, D. S., et al. 2018, in 1st Annual RPI Workshop on Image-Based Modeling and Navigation for Space Applications (Troy, NY)
Preusker, F., Scholten, F., Matz, K.-D., et al. 2015, A&A, 583, A33
Rizk, B., Drouet d'Aubigny, C., Golish, D., et al. 2018, SSRv, 214, 26
Rousseeuw, P. J. 1984, J. Am. Stat. Assoc., 79, 871
Rousseeuw, P. J., & Driessen, K. V. 1999, Technometrics, 41, 212
Rowlands, D., Pavlis, D., Lemoine, F., Neumann, G., & Luthcke, S. 1999, GeoRL, 26, 1191
Sahr, E., Pelgrift, J., Nelson, D., et al. 2022, in AIAA SciTech Forum 2022 (Reston, VA: AIAA) AIAA 2022-2519
Scheeres, D., French, A., Tricarico, P., et al. 2020, SciA, 6, eabc3350
Scheeres, D., McMahon, J., French, A., et al. 2019, NatAs, 3, 352
Seabrook, J., Daly, M., Barnouin, O., et al. 2019, P&SS, 177, 104688
Seabrook, J. A., Daly, M. G., Barnouin, O. S., et al. 2022, PSJ, 3, 265
Semenov, B. & NAIF 2019, OSIRIS-REx (ORX) Frames Kernel, v1.4, https://naif.jpl.nasa.gov/pub/naif/ORX/kernels/fk/orx_v14.tf
Slobin, S. D. 2022, Deep Space Network, 810-005, 301, https://deepspace.jpl.nasa.gov/dsndocs/810-005/301/301N.pdf
Williams, B., Antreasian, P., Carranza, E., et al. 2018, SSRv, 214, 69
Xiao, H., Stark, A., Steinbrügge, G., Hussmann, H., & Oberst, J. 2021, JGeod, 95, 22